Neural activity induces strongly coupled electro-chemo-mechanical interactions and fluid flow in astrocyte networks and extracellular space – a computational study

Marte J. Sætra[1,*], **Ada J. Ellingsrud**[1], **and Marie E. Rognes**[1]

[1]Department of Numerical Analysis and Scientific Computing, Simula Research Laboratory, Kristian Augusts gate 23, 0164 Oslo, Norway

[*]Corresponding author: martejulie@simula.no

ABSTRACT

The complex interplay between chemical, electrical, and mechanical factors is fundamental to the function and homeostasis of the brain, but the effect of electrochemical gradients on brain interstitial fluid flow, solute transport, and clearance remains poorly quantified. Here, via in-silico experiments based on biophysical modeling, we estimate water movement across astrocyte cell membranes, within astrocyte networks, and within the extracellular space (ECS) induced by neuronal activity, and quantify the relative role of different forces (osmotic, hydrostatic, and electrical) on transport and fluid flow under such conditions. Our results demonstrate how neuronal activity in the form of extracellular ionic input fluxes may induce complex and strongly-coupled chemical-electrical-mechanical interactions in astrocytes and ECS. Furthermore, we observe that the fluid dynamics are crucially coupled to the spatial organization of the intracellular network, with convective and electrical drift dominating ionic diffusion in astrocyte syncytia.

Author Summary

Over the last decades, the neuroscience community has paid increased attention to the astrocytes – star-shaped brain cells providing structural and functional support for neurons. Astrocyte networks are likely to be a crucial pathway for fluid flow through brain tissue, which is essential for the brain's volume homeostasis and waste clearance. However, numerous questions related to the role of osmotic pressures and astrocytic membrane properties remain unanswered. There are also substantial gaps in our understanding of the driving forces underlying fluid flow through brain tissue. Answering these questions requires a better understanding of the interplay between electrical, chemical, and mechanical forces in brain tissue. Due to the complex nature of this interplay and experimental limitations, computational modeling can be a critical tool. Here, we present a high

fidelity computational model of an astrocyte network and the extracellular space. The model predicts the evolution in time and distribution in space of intra- and extracellular volumes, ion concentrations, electrical potentials, and hydrostatic pressures following neural activity. Our findings show that neural activity induces strongly coupled chemical-mechanical-electrical interactions in the tissue and suggest that chemical gradients inside astrocyte syncytia strengthen fluid flow at the microscale.

1 Introduction

The complex interplay between chemical, electrical, and mechanical factors is fundamental to central nervous system physiology [1, 2, 3] and pathologies such as edema and stroke [4], vascular dementia, and neurodegenerative disease [5, 6], as well as in cortical tissue engineering [7]. Movement of ions between neuronal, glial, and extracellular spaces underpin membrane depolarization and thus the electrical activity of excitable cells [8, 9, 10]. On the other hand, chemical gradients induce osmotic pressures forcing water across the semi-permeable cellular membranes [11, 12, 13], challenging their volume homeostasis and inducing hydrostatic pressure gradients within each compartment. Simultaneously, the pulsating mechanical forces of the cardiovascular system act on this environment at the neuro-vascular and glio-vascular interfaces.

The renewed interest in brain clearance pathways over the last decade, supported by breakthroughs in imaging [14], experimental discoveries [15, 16], and the potential of computational modeling, has brought new relevance and new perspectives to this intriguing interplay. Key open questions relate to the role of astrocytes in brain signaling, volume homeostasis, and clearance in general [3, 16], and the role of osmotic pressures and astrocytic membrane properties on brain solute transport in particular. Specifically, there are substantial gaps in our understanding of (i) the driving forces underlying interstitial fluid movement and (ii) biophysical mechanisms for how astrocyte membrane features such as AQP4- and KIR-channels or NKCC1 co-transporters contribute to perivascular or interstitial transport [3, 16, 17, 18, 19, 20].

These questions seem intrinsically related to interactions between mechanical and chemical forces, and molecular diffusion juxtaposed with electrical and advective drift, but have largely not been addressed as such. The focus in computational neuroscience has conventionally been on electrophysiology alone [21], predominantly neglecting intracellular or extracellular ionic gradients [22]. In turn, even models at extreme morphological detail of intracellular and extracellular diffusion and reactions tend to ignore electrical drift and fluid mechanics [23, 24]. Moreover, while there has been a surge of computational fluid dynamics studies of the magnitude and mechanisms of cerebrospinal fluid flow, perivascular fluid flow [25, 26], and interstitial fluid flow [27, 28, 29] and their effect on brain solute transport [30, 31, 32, 33], almost all ignore electro-chemical and osmotic effects.

In Halnes et al. [34], the authors introduce an electrodiffusive framework for modeling ion concentrations in astrocytes and extracellular space along one spatial dimension while ignoring mechanical aspects such as cellular swelling and compartmental fluid dynamics. By modeling ionic concentrations in intra- and extracellular compartments, Østby et al. [35] and later Jin et al. [36] study the interplay between astrocytic membrane mechanisms, transmembrane water movement, and extracellular space shrinkage in connection with neuronal activity. Neither of these latter models [35, 36] include a spatial dimension and thus do

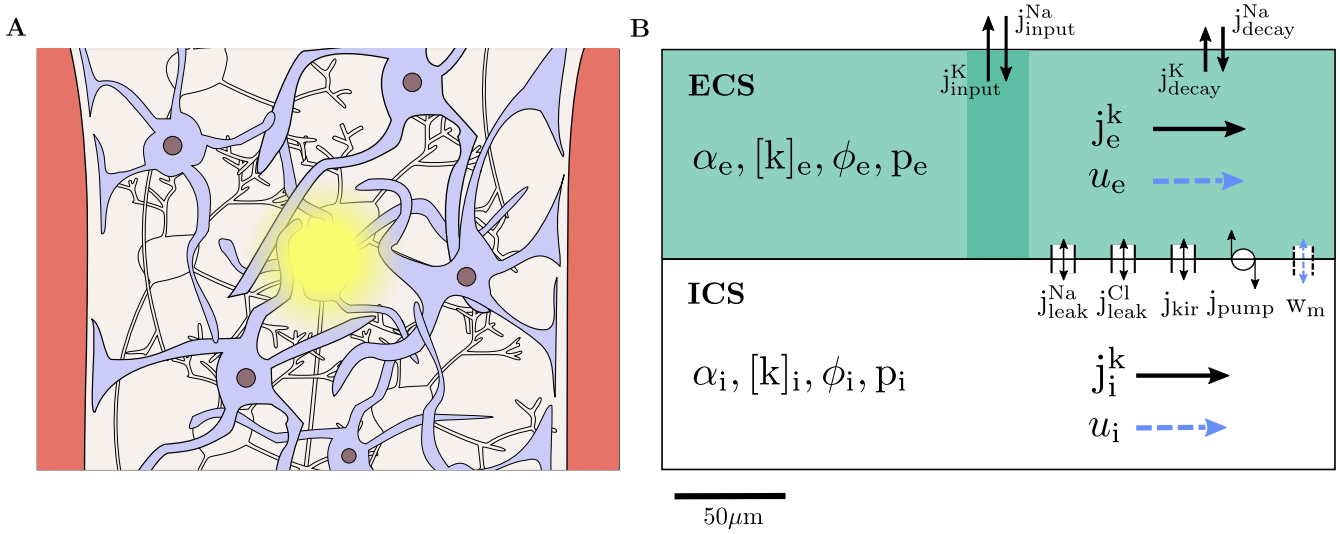

Figure 1. Model schematics. Illustration of brain tissue between two blood vessels with astrocytes (purple), neurons (grey), and ECS with neural activity in the center (**A**). The tissue is represented as a 1D domain of length 300 μm including ICS (astrocytes) and the ECS (**B**). Within each compartment, the model describes the dynamics of the volume fraction (α), the Na^+ , K^+, and Cl^- concentrations ($[Na^+]$, $[K^+]$, $[Cl^-]$), the electrical potential (ϕ), and the hydrostatic pressure (p). Neuronal activity is implicitly represented by K^+ and Na^+ input currents (j^K_{input} and j^{Na}_{input}) in the input zone (of length 30 μm) and decay currents (j^K_{decay} and j^{Na}_{decay}) across the whole domain. Transmembrane currents include an inward rectifying K^+ current (j_{Kir}), Na^+ and Cl^- leak currents (j^K_{leak} and j^{Cl}_{leak}), and a Na^+/K^+ pump current (j_{pump}). Intra- and extracellular currents (j^k_i and j^k_e) are driven by electrodiffusion and advection. Fluid can travel across the membrane (w_m) and compartmentally in the intra- and extracellular space (u_i and u_e).

not account for intra-compartmental gradients. In pioneering work, Asgari and collaborators [37] study how astrocyte networks may modulate extracellular fluid flow and transport given a hydrostatic pressure difference between paraarterial and paravenous spaces via a spatially-discrete electrical analog model. A unifying framework fully incorporating spatial and temporal dynamics of both ionic electrodiffusion and fluid movement in an arbitrary number of compartments is presented by Mori [38]. In this framework, hydrostatic and osmotic pressure gradients are assumed to drive fluid flow in both intra- and extracellular spaces. Zhu et al. [39] later extend this framework by including electro-osmosis as a driving force for interstitial fluid movement. They apply their framework to study the role of fluid flow on ionic transport in the optical nerve. However, little attention has been paid to quantifying the contributions of different driving forces for interstitial fluid flow during neuronal activity in the cortex.

Here, our target is two-fold: we aim to estimate the water movement induced by neuronal activity across astrocyte cell membranes, within astrocyte networks, and within the extracellular space, and to determine the relative role of different forces (osmotic, hydrostatic, and electrical) on ionic transport and fluid flow under such conditions. To estimate this electro-chemo-mechanical response, we introduce a high-fidelity computational model describing the spatial and temporal dynamics at the micro/milliscale of volume fractions, electrical potentials, ion concentrations, and hydrostatic pressures in an intracellular space (ICS) representing different astrocyte configurations and the extracellular space (ECS) (Figure 1). The model is embedded in the electrodiffusive Kirchhoff-Nernst-Planck framework and builds on previous work [40] incorporating ionic electrodiffusion [34, 38], fluid dynamics [39], and astrocyte modeling [34].

Our findings show that neuronal activity in the form of extracellular ionic input fluxes induces complex and strongly-coupled chemical-electrical-mechanical interactions in the astrocytic ICS and ECS. The response is characterized by membrane (electric) potential depolarization on the order of tens of millivolts and ECS water potentials ranging from a few to a hundred kilo-pascals, spatial differences in osmolarity on the order of several tens of millimolars, and fluid velocities ranging from a fraction – to tens of micrometers per minute. The fluid dynamics are crucially coupled to the spatial organization of the intracellular network, with convective and electrical drift dominating ionic diffusion in astrocyte syncytia.

2 Results

In order to quantify the relative role of osmotic, hydrostatic, and electrical forces on transport and flow in cortical tissue, we ask the following questions. How do astrocyte and extracellular ion concentrations, electric potentials, pressures, and interstitial fluid velocities respond to changes in extracellular ion concentrations mirroring neural activity on the time scale of seconds? Moreover, to what extent do the mechanical responses (cellular swelling, fluid flow) contribute to alleviating ionic and mechanical ECS distress? To address these questions, we introduce a set of biophysical models for these quantities of interest, governed by the balance of mass, momentum, and charge, in combination with astrocyte membrane mechanisms in a representative volume.

2.1 A model for electrodiffusive, osmotic, and hydrostatic interplay in astrocyte networks

Ion- and fluid movement in an astrocyte network (ICS) and the extracellular space (ECS) is modeled via coupled partial differential equations (PDEs) in a homogenized model domain (Figure 1, Methods). Specifically, we consider a 1D domain of length 300 µm representing brain tissue between two blood vessels, e.g., an arteriole and a venule. The model predicts the evolution in time and distribution in space of the volume fraction α_r, the ion concentrations $[Na^+]_r$, $[K^+]_r$, and $[Cl^-]_r$, the electrical potential ϕ_r, and the hydrostatic pressure p_r in both ICS ($r =$i) and ECS ($r =$e). Ionic transport is driven by diffusion, electric drift, and advection. To model fluid movement in each compartment, we consider three different model scenarios:

M1 The intra- and extracellular fluid flow is driven by hydrostatic pressure gradients. The astrocytic compartment can be interpreted as either a single closed cell or as a syncytium of cells without intercellular osmotic flow.

M2 The intracellular fluid flow is driven by osmotic and hydrostatic pressure gradients, and the extracellular fluid flow is driven by the same mechanism as in M1. The astrocytic compartment can be interpreted as a syncytium of cells where osmosis acts as a driving force for fluid flow.

M3 The intracellular fluid flow model is the same as in M2, and the extracellular fluid flow is driven by electro-osmosis in addition to hydrostatic pressure gradients. To include electro-osmosis as a driving force for ECS fluid flow is motivated by the narrowness of the ECS [39, 41].

For comparison, we also consider a zero-flow scenario [34]:

M0 The compartmental fluid velocities and the transmembrane fluid flow (and thus cellular swelling) are assumed to be zero.

Transmembrane fluid flow in model scenarios M1–M3 is driven by hydrostatic and osmotic pressure differences. At the boundaries, we assume that no fluid and no ionic fluxes enter or leave the system. To account for transmembrane ionic movement, we include an inward rectifying K^+ channel, passive Na^+ and Cl^- channels, and a Na^+/K^+ pump. To ensure electroneutrality of the system, we include a set of immobile anions a_r. The immobile anions contribute to the osmotic pressures.

We mimic a scenario of high local neuronal activity by injecting a constant K^+ current into the ECS and simultaneously removing Na^+ ions in a stimulus zone in the middle of the computational domain. To maintain electroneutrality of the system, the K^+ and Na^+ input currents are of the same magnitude. Neuronal pumps and cotransporters are accounted for by removing K^+ ions from the ECS at a given decay rate and adding the same amount of Na^+ ions. The decay is proportional to the extracellular K^+ concentration and defined across the whole domain. Note that the stimulus does not induce any osmotic pressure changes, as it does not affect the total osmotic concentration of the ECS.

2.2 Neuronal activity induces complex chemical-electrical-mechanical interplay

In order to understand and quantify the baseline electrical and mechanical response to chemical alterations, we first consider the model scenario where the compartmental fluid flow is only driven by hydrostatic pressure gradients (M1). Turning on the input currents at $t = 10\,\mathrm{s}$ leads to changes in the ion concentrations, cellular swelling, depolarization of the glial membrane, and an increase in the transmembrane hydrostatic pressure difference. After about 40 seconds, the system reaches a new steady state, before all fields return to baseline levels after input offset at $t = 210\,\mathrm{s}$ (Figure 2).

The input currents (Figure 2A) and the subsequent astrocytic activity lead to an increase of 6.68 mM in $[K^+]_e$, a decrease of 18.7 mM in $[Na^+]_e$, and a decrease of 16.9 mM in $[Cl^-]_e$, measured at the center of the input zone (Figure 2C). The increase in $[K^+]_e$ activates the K^+- and Na^+-decay currents (Figure 2B), which eventually lead the system back to baseline. Intracellularly, we observe an initial peak in $\Delta[K^+]_i$ of 3.19 mM before it settles on 0.428 mM. $[Na^+]_i$ and $[Cl^-]_i$ decrease by 6.44 mM and increase by 6.55 mM, respectively (Figure 2D). In response to the ionic shifts, the astrocytic compartment swells: the ICS volume increases by 13 % (Figure 2F) and the ECS shrinks correspondingly by 26 % (Figure 2E). As the initial size of the ECS is half that of the ICS, a change in ECS volume twice that of the ICS volume is as expected. Further, these volume changes affect the hydrostatic pressures: the transmembrane hydrostatic pressure difference increases by 118 Pa (Figure 2G). Finally, the glial membrane potential depolarizes from $-86\,\mathrm{mV}$ to $-61\,\mathrm{mV}$ (Figure 2H).

2.3 Transmembrane dynamics induce hydrostatic pressure gradients and compartmental fluid flow

Osmotically driven transport of fluid through AQP4, and possibly other membrane mechanisms, play an important role in cellular swelling and volume control of the ECS [42, 43, 44, 45]. Whether cellular swelling induces hydrostatic pressure gradients driving compartmental fluid flow in the ICS and ECS is, however, far from settled [34]. We therefore also assess to what extent osmotic pressures induce hydrostatic pressures and fluid flow, still in the model scenario with hydrostatic-pressure-driven

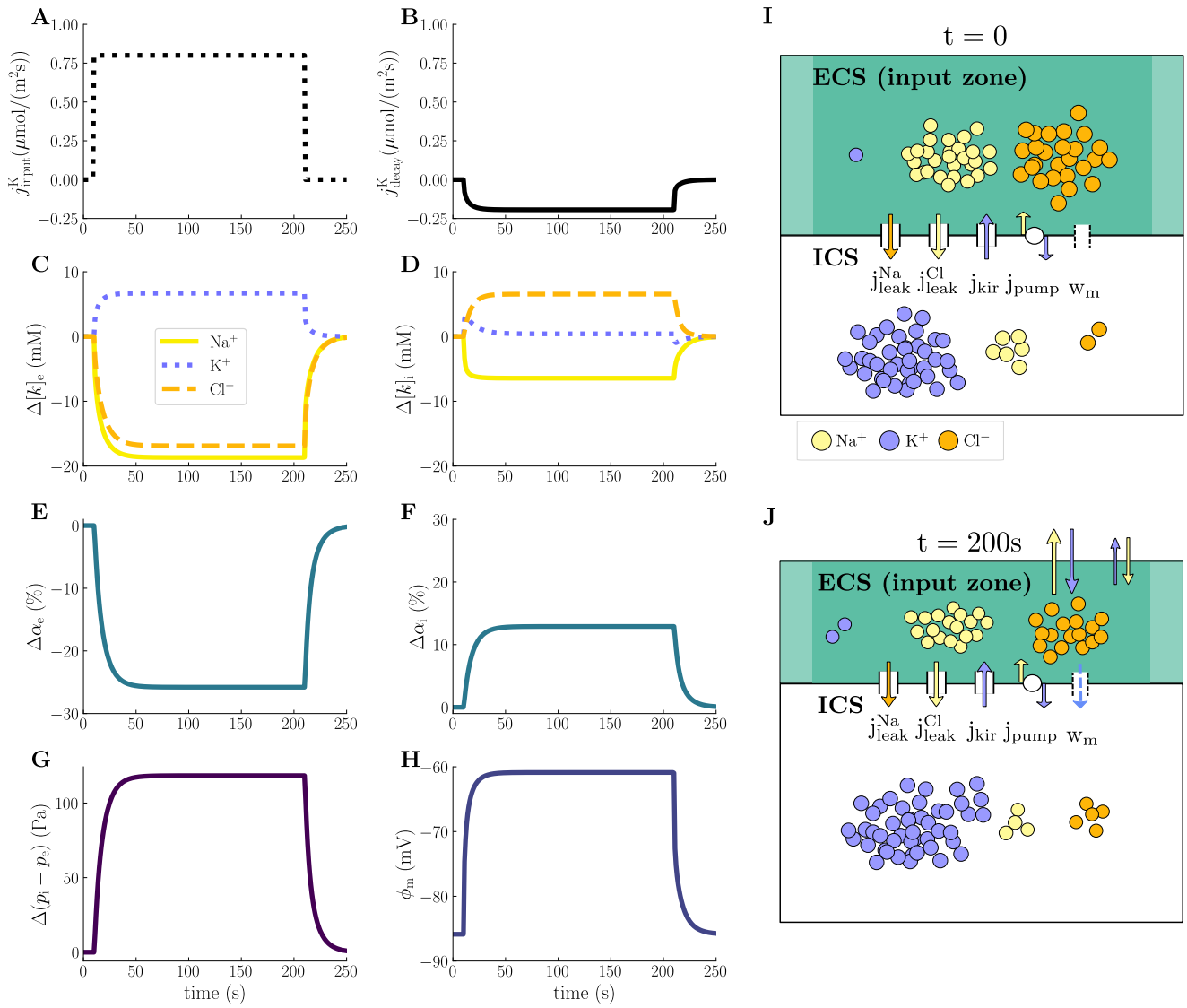

Figure 2. Electrical, chemical, and mechanical dynamics in the input zone during local neuronal activity. The panels display the time evolution of the K^+-injection current (**A**) and K^+-decay current (**B**), changes in the ECS (**C**) and ICS (**D**) ion concentrations, changes in the ECS (**E**) and ICS (**F**) volume fractions, changes in the transmembrane hydrostatic pressure difference (**G**), and membrane potential (**H**) at $x = 150\,\mu$m (center of the input zone). All changes are calculated from baseline values, which are listed in Methods. Panel **I** and **J** display a schematic overview of ionic dynamics and swelling at respectively $t = 0\,$s and $t = 200\,$s at $x = 150\,\mu$m.

compartmental fluid flow (M1).

The concentration shifts following astrocytic activity result in altered ICS and ECS osmolarities. Notably, the change in osmolarities peak in the input zone, where the intra- and extracellular osmolarities decrease by maximum 20.5 mM and 20.7 mM, respectively (Figure 3A). Consequently, the osmotic pressure across the astrocytic membrane decreases by a maximum of 713 Pa (Figure 3B). The osmotic pressure drives fluid across the astrocytic membrane, with a maximum velocity of 0.003 μm/min (Figure 3C), resulting in cellular swelling. Following swelling, the ICS hydrostatic pressure increases by at most 21.2 Pa in the input zone, while the ECS hydrostatic pressure drops by at most 97.1 Pa (Figure 3D). Note that the changes

in compartmental hydrostatic pressures lead to a change in the transmembrane hydrostatic pressure gradient (Figure 3B), which affects the transmembrane fluid flow.

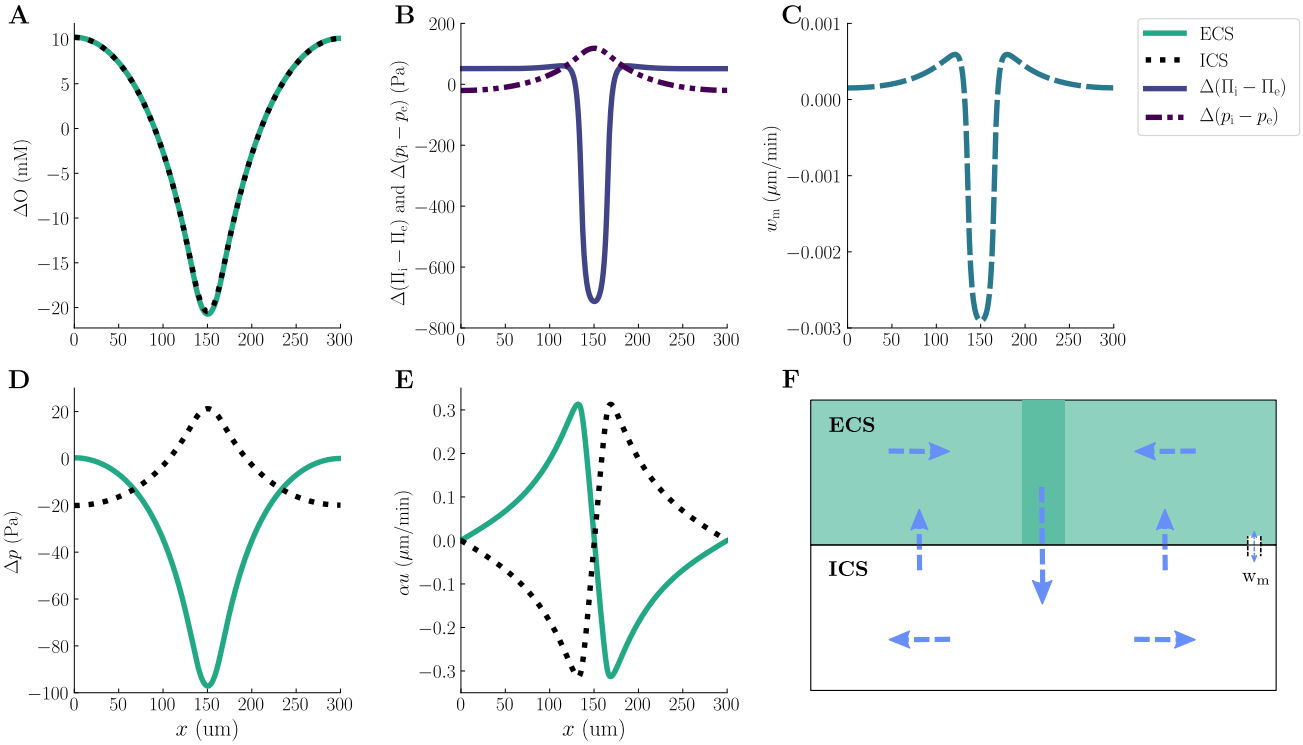

Figure 3. Interplay between transmembrane- and compartmental pressures and fluid velocities (M1). The panels display a snapshot (at $t = 200$ s) of the spatial distribution of the changes in intra- and extracellular osmolarities (**A**), osmotic and hydrostatic pressure gradients across the glial membrane (**B**), transmembrane fluid velocity (**C**), changes in the intra- and extracellular hydrostatic pressures (**D**), intra- and extracellular superficial fluid velocities (**E**), and illustration of the flow pattern (**F**). All changes are calculated from baseline values, which are listed in Methods.

The ICS and ECS hydrostatic pressure gradients drive compartmental fluid flow forming two circulation zones (Figure 3E,F). The intra- and extracellular superficial fluid velocities, $\alpha_r u_r$, peak at 0.31 μm/min (Figure 3E). Note that the two superficial fluid velocities are opposite in direction but have the same magnitude – this is a direct consequence of the incompressibility condition and no-flux boundary conditions in one dimension. During steady-state and cellular swelling in the input zone, fluid flows across the membrane into the ICS (Figure 3C). In the ICS, the fluid consequently flows away from the input zone, with positive flow to the right of the swelling and negative flow to the left of the swelling (Figure 3E). The ECS fluid flow is in the opposite direction, towards the input zone (Figure 3E).

2.4 Extracellular and intracellular fluid flow alleviate osmotic pressure build-up

In a previous study [46], we predicted the strength of osmotic pressure build-up across an astrocyte membrane using a classical electrodiffusive model not accounting for fluid flow. However, to what extent will swelling and compartmental fluid flow affect osmotic pressure build-up across the membrane? Here, we investigate this question by comparing predictions of the zero-flow model (M0), the flow model without intercellular osmotic flow (M1), and the flow model with osmotic intercellular flow (M2).

The ICS and ECS osmolarities are altered by astrocytic activity in all model scenarios, notably peaking in the input zone (Figure 4A,B). In the ECS, the osmolarity decrease by 36.5 mM, 20.7 mM, and 6.74 mM for M0, M1, and M2, respectively (Figure 4A). Interestingly, the ICS osmolarity increases by 10.5 mM and 1.09 mM for M0 and M2, respectively, whereas it decreases for model scenario M1 by 20.45 mM (Figure 4B). The decrease in ICS osmolarity in model scenario M1 results from cellular swelling: the osmolarity is defined as the amount of ions per unit volume. An increase in cell volume may thus cause the ion concentration to drop even if the number of ions increases. Furthermore, we can convert the intra- and extracellular osmolarities to intra- and extracellular solute potentials, Π_i and Π_e, respectively (see Section 4.2 for further details). Taking the difference in solute potential across the membrane gives us the osmotic pressure, which differs substantially between the models: M0, M1, and M2 predict a maximum drop in osmotic pressure of respectively 121 kPa, 0.713 kPa, and 20.2 kPa (Figure 4C). Allowing for cellular swelling and compartmental fluid flow thus reduces the osmotic pressure across the membrane by 99.4 % (M1) and 83.3 % (M2). These findings suggest that model scenario M0, or generally any model for electrodiffusion not taking into account fluid dynamics, highly overestimates the osmotic pressure building up across the membrane.

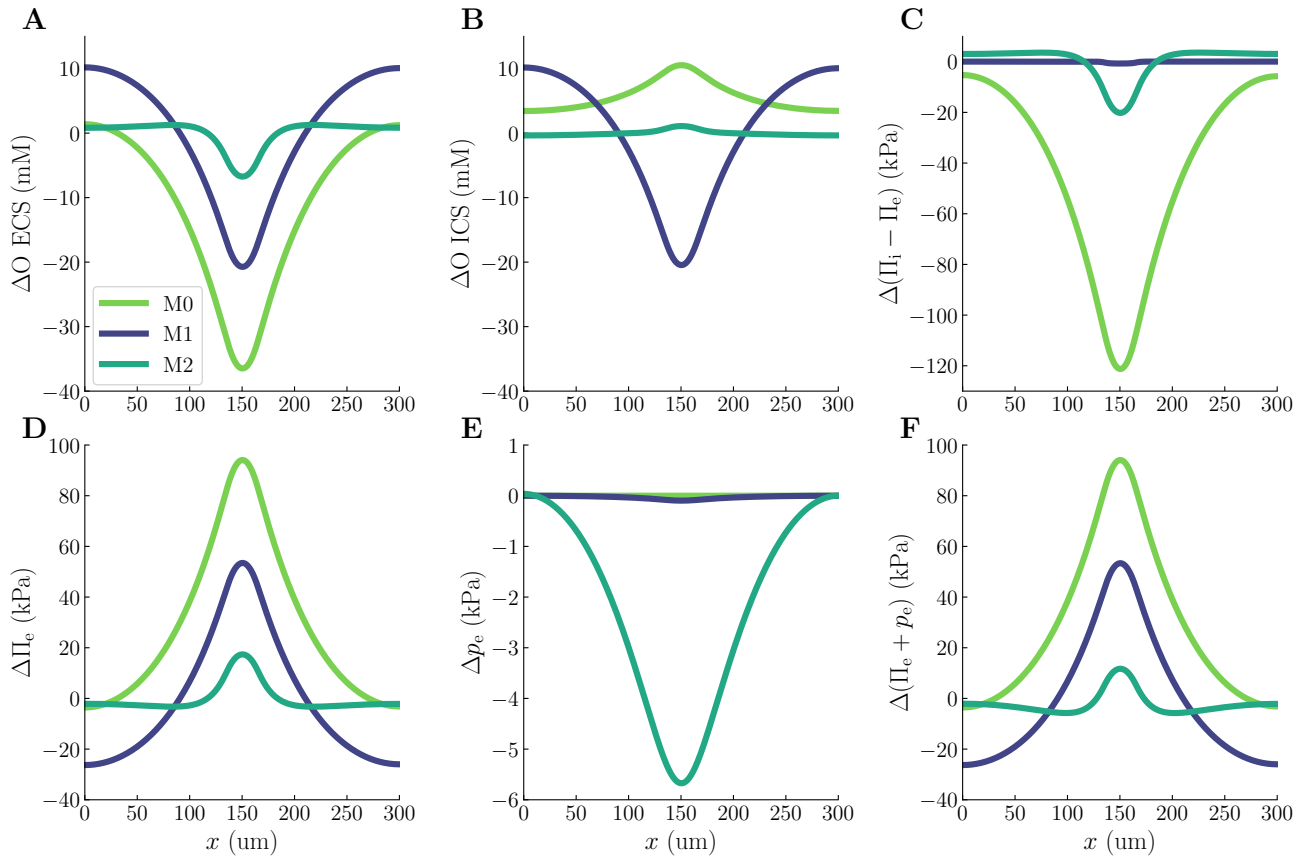

Figure 4. Comparison of osmotic pressures and ECS water potentials predicted by model scenarios M0, M1, and M2. The upper panels display a snapshot of ICS osmolarities (**A**), ECS osmolarities (**B**), and osmotic pressures across the membrane (**C**). The lower panels display a snapshot of ECS solute potentials (**D**), ECS hydrostatic pressures (**E**), and ECS water potentials (**F**). All panels display the deviation from baseline levels at $t = 200$ s.

2.5 Volume dynamics is essential for ECS homeostasis

Water uptake in astrocytes via e.g. AQP4 has been hypothesized to contribute to stabilize ECS ion concentrations, and thus prevent severe neuronal swelling. Swelling is driven by the difference in intra- and extracellular water potential, which is given by the solute potential Π_r plus the hydrostatic pressure p_r (see Methods for details). An increase in extracellular water potential will result in neuronal swelling as water flows along the potential gradient.

For all model scenarios (M0, M1, M2), the ECS solute potential increases (Figure 4D). The increase is most severe for the zero-flow model (M0), which predicts a maximum increase of 94.1 kPa. When taking swelling and compartmental hydrostatic-pressure-driven fluid flow into account (M1), the ECS solute potential increases by maximum 53.5 kPa, whereas adding ICS osmotic forces (M2) leads to an increase of maximum 17.4 kPa. In M0, the change in p_e is zero by definition, whereas M1 predicts a negligible maximal drop (0.0971 kPa, Figure 4E). Conversely, model scenario M2 predicts a pronounced hydrostatic pressure drop (5.67 kPa, Figure 4E). Consequently, the maximal change in the ECS water potential is substantially smaller in M2 (11.7 kPa, Figure 4F) than in M0 and M1 (respectively 94.1 kPa and 53.4 kPa, Figure 4F). The maximal change in the ECS solute potential is less severe for M2 than for M0 and M1 (Figure 4D). Additionally, while the ECS solute potentials increase (Figure 4D), the ECS hydrostatic pressures decrease (Figure 4E), and thus drive the water potential in opposite directions. Consequently, the ECS hydrostatic pressure change in M2 reduces the contribution from the less severe change in ECS solute potential, resulting in a lower ECS water potential. Thus, cellular swelling and osmotic transport within the astrocytic network (M2) contribute to prevent water potential build-up in the ECS.

2.6 Astrocyte osmotics strengthens compartmental fluid flow

The presence of driving forces for fluid flow – both at the brain microscale and organ-level – remain an open question. To assess the potential contributions from osmosis in the astrocytic network (M2) and electro-osmosis in the ECS (M3), we here compare the compartmental fluid velocities, cellular swelling, and hydrostatic pressures predicted by model scenarios M1, M2, and M3.

The maximum superficial fluid velocity predicted by M2 is 14 μm/min – about 45 times larger than for M1 (Figure 5A,B and Table 1). For M3, the maximum superficial fluid velocity is 13 μm/min – slightly smaller than for M2 (Figure 5C,D and Table 1). For both M2 and M3, the fluid velocities are dominated by osmosis in the ICS (Figure 5A,C) and hydrostatic forces in the ECS (Figure 5B,D). Interestingly, the intracellular hydrostatic pressure gradient drives fluid towards the input zone in M2 and M3 (Figure 5A,C), as opposed to the intracellular hydrostatic pressure in M1 which drives fluid away from the input zone (Figure 3C). The difference in ICS flow direction predicted by M1, M2, and M3 arises from the coupling of the hydrostatic-, osmotic-, and electro-osmotic forces in the mathematical model: the osmotic- and electro-osmotic forces are given by the ion concentration- and electrical potential gradients, respectively, whereas the hydrostatic pressure result from the incompressibility of the interstitial fluid (cf. Equation (7)). Less cellular swelling is predicted by M2 and M3 than by M1: the astrocyte swells by respectively 12.9 %, 3.74 %, and 4.55 % in M1, M2, and M3 (Table 1). Finally, we observe notable differences in the intra- and extracellular hydrostatic pressures: the maximum ICS hydrostatic pressure is 1.02 kPa, −4.64 kPa, and −10.3 kPa in M1, M2, and M3, respectively (Table 1). The maximum ECS hydrostatic pressure is −0.0971 kPa, −5.67 kPa, and −11.3 kPa in M1,

M2, and M3, respectively (Table 1). The transmembrane hydrostatic pressures are similar in M2 and M3 even if the intra- and extracellular pressures are different: the maximum transmembrane hydrostatic pressure is respectively 1.03 kPa and 1.04 kPa in M2 and M3 (Table 1). The maximum transmembrane hydrostatic pressure in M1 is 1.12 kPa (Table 1).

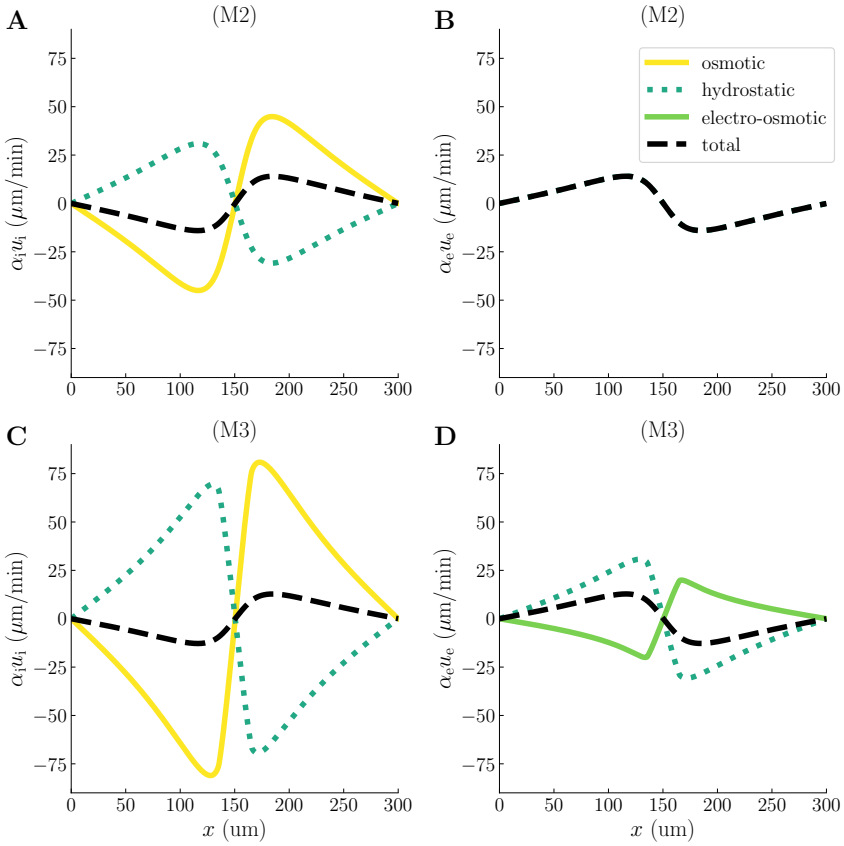

Figure 5. Fluid velocities predicted by model scenarios M2 and M3. Spatial profiles of the total superficial fluid velocities (black dashed lines), together with their hydrostatic (dotted green lines), osmotic (yellow line), and electro-osmotic (solid green line) contributions at $t = 200$ s. The upper panels show the intra- **(A)** and extracellular **(B)** fluid velocities for model scenario M2. The lower panels show the intra- **(C)** and extracellular **(D)** fluid velocities for model scenario M3.

2.7 Astrocyte osmotics accelerates ionic transport and alters role of advection

In model scenarios M1–M3, the compartmental fluid velocities will contribute to ionic transport via advection. To assess the role of advection in compartmental ionic transport, we compare model scenarios M1 and M3. Specifically, we decompose the intra- and extracellular ionic fluxes and calculate the advection/diffusion fraction (F_{diff}) and the advection/drift fraction (F_{drift}) for each of the ionic species (see Methods for further details).

We observe that F_{diff} and F_{drift} range from 0.002 to 0.062 in model scenario M1, indicating that advection plays a negligible role in ionic transport (Figure 6A-F). In model scenario M3, however, we observe a larger variability in the advection/diffusion- and advection/drift rates: F_{diff} ranges from 0.058 to 4.519, and F_{drift} ranges from 0.325 to 0.949 (Figure 6G-L). For K^+ transport in the M3 model, the advective flux is on the same order of magnitude as the intra- and extracellular electric drift

Table 1. Quantities of interest for the different model scenarios (M0, M1, M2, and M3). All measurements are taken at $t = 200\,\mathrm{s}$ and at $x = 150\,\mu\mathrm{m}$, except from the max ICS- and ECS intrinsic fluid velocities (u_r) and the max ICS- and ECS superficial fluid velocities ($\alpha_r u_r$) which are the maximum values over space at $t = 200\,\mathrm{s}$. (–) denotes that the value is not applicable.

Model scenario	M0	M1	M2	M3
ICS swelling (%)	–	12.9	3.74	4.55
ECS shrinkage (%)	–	25.8	7.48	9.12
ICS osmolarity (mM)	315	283.9	305	303
ECS osmolarity (mM)	268	283.3	297	296
Osmotic pressure (kPa)	−122	−1.71	−21.2	−19.4
ICS hydrostatic pressure (kPa)	–	1.02	−4.64	−10.3
ECS hydrostatic pressure (kPa)	–	−0.0971	−5.67	−11.3
Transmembrane hydrostatic pressure difference (kPa)	–	1.12	1.03	1.04
max ICS intrinsic fluid velocity (µm/min)	–	0.71	34	31
max ECS intrinsic fluid velocity (µm/min)	–	2.0	75	69
max ICS superficial fluid velocity (µm/min)	–	0.31	14	13
max ECS superficial fluid velocity (µm/min)	–	0.31	14	13
Transmembrane fluid velocity (µm/min)	–	−0.0029	−0.099	−0.090

and about 4.5 times stronger than the intracellular diffusion ($F_{\mathrm{diff}} = 4.519$, Figure 6G,J). Advection plays the most important role intracellularly and accelerates the K^+ transport; For M1, the intracellular K^+ flux has a maximum value of $58\,\mu\mathrm{mol}/(\mathrm{m}^2\mathrm{s})$ (Figure 6D), whereas for M3, the maximum intracellular K^+ flux is $70\,\mu\mathrm{mol}/(\mathrm{m}^2\mathrm{s})$ (Figure 6J). For Na^+ and Cl^- transport in the M3 model, advection is on the same order of magnitude as diffusion and electric drift (Figure 6H,I,K,L). The advection even dominates intracellular diffusion of Na^+ ($F_{\mathrm{diff}} = 1.286$, Figure 6K) and extracellular diffusion of Cl^- ($F_{\mathrm{diff}} = 4.079$, Figure 6I). Overall, advection accelerates the transport of total charge in the system: For M1, the charge flux (defined here as $z_{\mathrm{K}} j_{\mathrm{K}} + z_{\mathrm{Na}} j_{\mathrm{Na}} + z_{\mathrm{Cl}} j_{\mathrm{Cl}}$) is maximum $59\,\mu\mathrm{mol}/(\mathrm{m}^2\mathrm{s})$, whereas for M3, the charge flux is maximum $71\,\mu\mathrm{mol}/(\mathrm{m}^2\mathrm{s})$.

2.8 Flow sensitivity to changes in permeability and stiffness

The magnitude of the compartmental fluid velocities $\alpha \cdot u$ is likely to depend on the choice of parameters. We thus perform a sensitivity analysis where we measure the maximum superficial fluid velocity for different values of the compartmental permeability κ, the membrane stiffness K_{m}, and the membrane water permeability η_{m} (Figure 7). Specifically, we compare the sensitivity of modeling setups M1 and M3 in order to assess whether the differences we have observed between the two are robust with respect to the parameter choices.

By increasing κ from $0.0\,\mathrm{m}^2/(\mathrm{Pa\,s})$ to $1 \cdot 10^{-12}\,\mathrm{m}^2/(\mathrm{Pa\,s})$ (with the default value set to $1.8375 \cdot 10^{-14}\,\mathrm{m}^2/(\mathrm{Pa\,s})$), the superficial fluid velocity increases from $0.0\,\mu\mathrm{m/min}$ to $7.1\,\mu\mathrm{m/min}$ for M1 and from $0.0\,\mu\mathrm{m/min}$ to $15\,\mu\mathrm{m/min}$ for M3 (Figure 7A). The superficial fluid velocity in M3 converges around $\kappa = 1.4 \cdot 10^{-13}\,\mathrm{m}^2/(\mathrm{Pa\,s})$, while the superficial fluid velocity in M1 continues to increase through $\kappa = 1 \cdot 10^{-12}\,\mathrm{m}^2/(\mathrm{Pa\,s})$. The difference between M1 and M3 in superficial fluid velocities decreases for κ values above the default parameter choice, but we still observe a notable difference of 215 % at $\kappa = 1 \cdot 10^{-12}\,\mathrm{m}^2/(\mathrm{Pa\,s})$. For κ values below the default parameter choice, the absolute difference between M1 and M3 fluid velocities decreases, but the relative difference increases. Increasing K_{m} from $0.0\,\mathrm{Pa}$ to $3000\,\mathrm{Pa}$ (with the default value set to

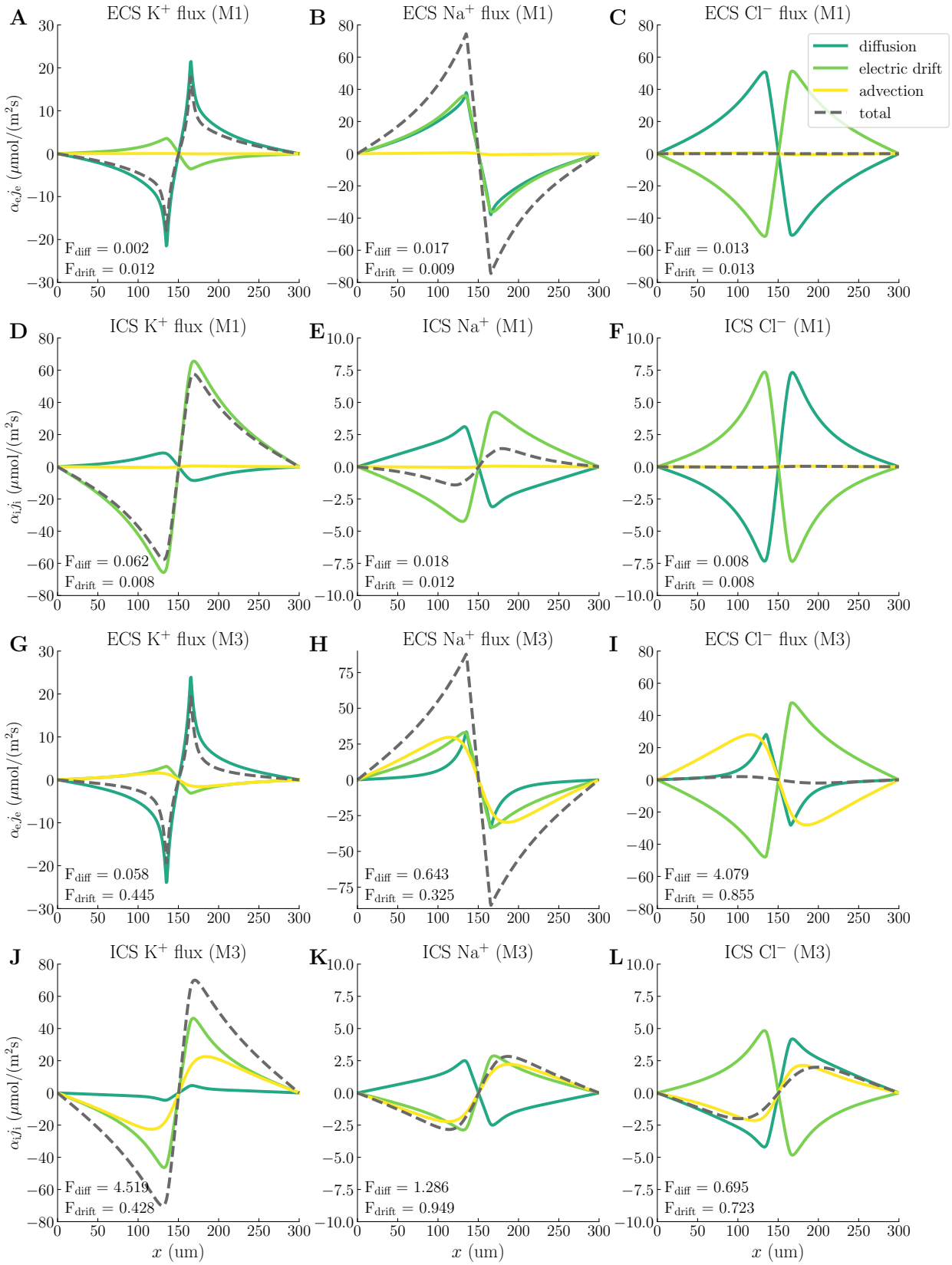

Figure 6. Compartmental ionic fluxes. Spatial profiles of the total compartmental ionic fluxes (grey dashed lines), and their diffusive (dark green lines), electric drift (light green lines), and advective (yellow lines) components at $t = 200$ s for the different ionic species. Each panel additionally contains the advection/diffusion fraction (F_{diff}) and the advection/electric drift fraction (F_{drift}) for the associated ion species. Panels **A-F** display fluxes for modeling scenario M1, and panels **G-L** display fluxes for modeling scenario M3. All fluxes are multiplied by the volume fraction α.

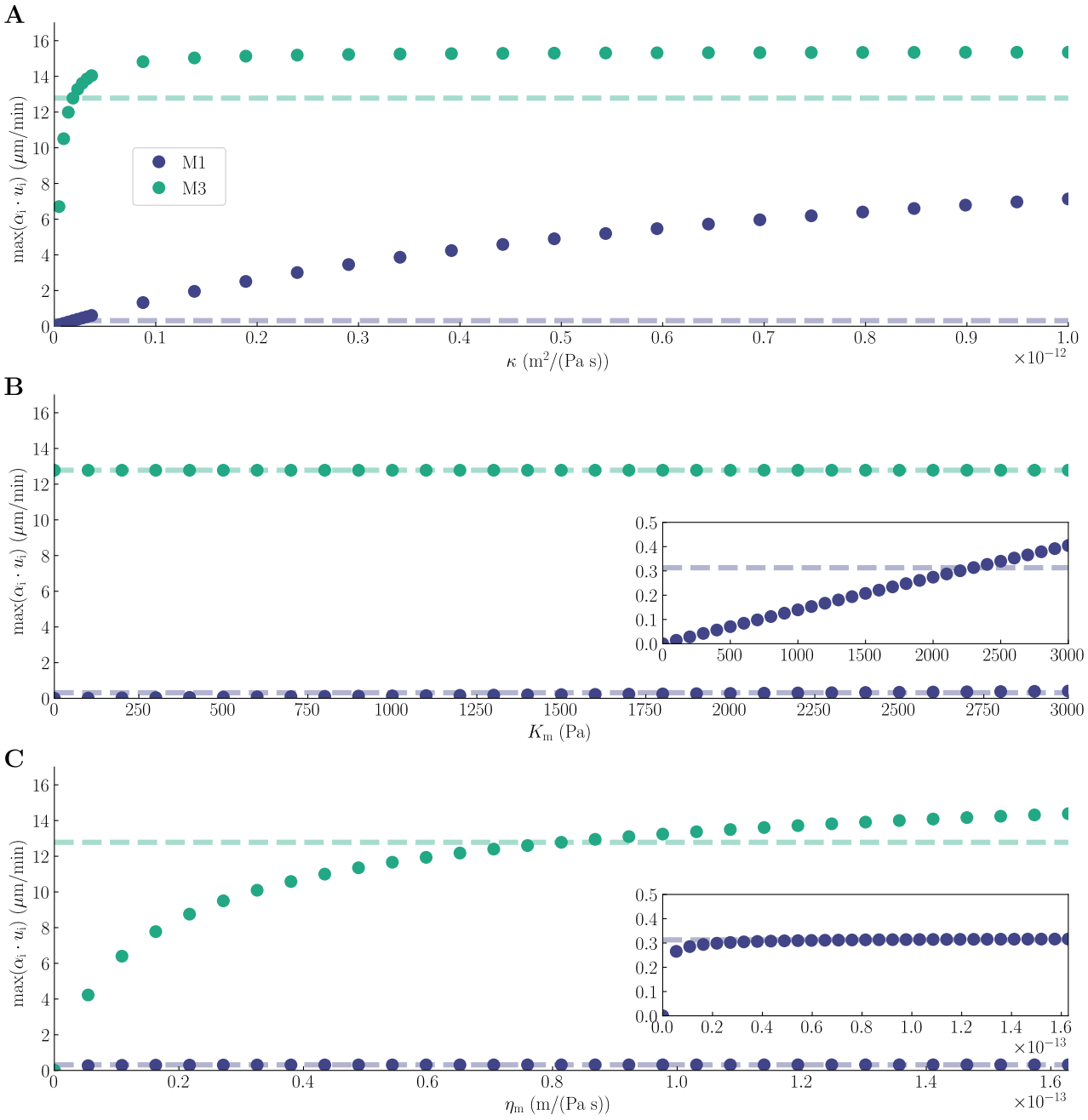

Figure 7. Sensitivity analysis. The maximum superficial fluid velocity, $\alpha_i u_i$, for different values of the compartmental permeability κ (**A**), membrane stiffness K_m (**B**), and membrane water permeability η_m (**C**) at $t = 200$ s for modeling scenarios M1 (blue dots) and M3 (green dots). The horizontal dashed lines mark the maximum value of $\alpha_i u_i$ corresponding to the default values of the model parameters. The default value of κ was set to be the same in the ICS and ECS, and we changed the two simultaneously by the same amount.

2294 Pa) increases the superficial fluid velocity linearly from 0.0 µm/min to 0.40 µm/min for M1 (Figure 7B). For M3, the superficial fluid velocity is 13 µm/min for all values of K_m. The small changes in M1 fluid velocities and constant M3 fluid velocity lead to a close-to-constant absolute difference between the predictions made by the two modeling setups when we vary K_m. By increasing the membrane water permeability η_m from 0.0 m/(Pas) to $1.628 \cdot 10^{-13}$ m/(Pas) (with the default value set to $8.14 \cdot 10^{-14}$ m/(Pas)), the superficial fluid velocity increases from 0.0 µm/min to 0.32 µm/min for M1 and from 0.0 µm/min to 14 µm/min for M3 (Figure 7C). The difference in superficial fluid velocity between M1 and M3 decreases for η_m values below the default choice, but we still observe that M3 predicts a 16 times higher superficial fluid velocity than M1 (4.2 µm/min vs. 0.27 µm/min) for η_m as low as $5.43 \cdot 10^{-15}$ m/(Pas).

3 Discussion

Our results demonstrate that localized extracellular K^+ influx in conjunction with Na^+ efflux, reflecting a zone of high neuronal activity, induces a strongly coupled and complex chemical-electrical-mechanical response in astrocyte ICS and the ECS with spatial and temporal changes in osmolarities, swelling, electrical potentials, pressures, and fluid flow. Cellular swelling and, importantly, osmotically driven fluid flow within the astrocytic network contribute to preventing high levels of extracellular water potential, effectively protecting against neuronal swelling. Fluid flow within each compartment may reach tens of µm/min and, as such, substantially contributes to the overall dynamics. Compartmental fluid flow, in concert with cellular swelling, alleviates osmotic pressure build-up and accelerates ionic transport within astrocytic networks by a factor of $\times 1$–5 compared to diffusion alone.

The shifts in ECS ion concentrations are in line with experimental observations and reports from comparable modeling studies. Experimentally, ECS K^+ is measured to increase by $6-12$ mM during sensory stimulation and strong electrical stimulation [2]. Halnes et al. [34, 47], Østby et al. [35], and Sætra et al. [48] report an increase in ECS K^+ in the range of $5-10$ mM via *in-silico* studies. We observe an increase in ECS K^+ of 6.68 mM in the input zone during stimuli. Further, we observe a decrease in both ECS Na^+ and Cl^- concentrations, which is in agreement with previous modeling studies [34, 47]. Interestingly, we observe a decrease in the ICS Na^+ concentration: although the number of Na^+ ions increases, the increase in ICS volume results in a total decrease in concentration. Our findings suggest that both ICS Cl^- and K^+ concentrations increase during neuronal activity. This is in agreement with previous experimental reports [49] and with K^+ uptake in astrocytes facilitating clearance of excess interstitial K^+ following neuronal activity [2].

Astrocytes swell in response to K^+ influx, reducing the interstitial space volume by up to 30% [42, 50, 51]. The local interplay between astrocytic K^+ uptake and ECS shrinkage has previously been studied computationally using single neuron-glia-ECS unit models, not considering spatial buffering [35, 36]. Østby et al. [35] report that inclusion of the co-transporters NBC and NKCC1, together with NKCC1-dependent water transport, is necessary to obtain ECS shrinkage that matches experimentally observed values. In their model scenario including only the major basic membrane processes (i.e., Na^+/K^+ pump, passive ion transport, and osmotically driven water transport), they obtain an ECS shrinkage of $10.8 \pm 4.0\%$. In contrast,

Jin et al. [36] report that their model accounts for experimental observations without including non-AQP4 water transport pathways. We observe a 25% shrinkage of the ECS with only passive transmembrane water transport during stimuli comparable to that of Østby et al. [35] and Jin et al. [36]

While the importance of osmotic effects has been widely recognized in the context of interstitial fluid flow and production, it has remained and remains hard to quantify [3, 16]. When prescribing a hydrostatic pressure difference of 1 mmHg/mm but ignoring electrochemical contributions and interactions between the ECS and ICS, Holter et al. [27] arrived at a superficial ECS fluid velocity estimate of less than 0.2 µm/min. Here, accounting for the combined biophysical effects of ionic electrodiffusion, cellular swelling, and fluid flow by hydrostatic and osmotic pressures, we estimate that neuronal activity may induce transmembrane fluid velocities on the order of 0.1 µm/min, intracellular fluid velocities in astrocyte networks of up to 14 µm/min, and fluid velocities in the ECS of similar magnitude. These velocities are dominated by an osmotic contribution in the intracellular compartment; without it, the estimated fluid velocities drop by a factor of $\times$34–45. Our estimates are very much in line with the interstitial bulk flow velocities of 5.5–14.5 µm/min [52, 53, 54], 10.5 µm/min [55], or 10.0 µm/min [56], as reported by Nicholson [57], the average interstitial bulk velocities in humans of 1–10 µm/min as quantified by Vinje et al. [32], and in the lower range of the 7–50 µm/min bulk flow velocities identified by Ray et al [58]. Comparing with the pioneering modeling study by Asgari et al. [37], they report baseline flow estimates resulting from a hydrostatic pressure difference (of unknown origin) alone of $\approx 1\text{–}3 \cdot 10^{-2} \mu m^3/s$. Interestingly, the intra-astrocytic and extracellular fluid velocities induced in our study result directly from the chemo-mechanical interactions following extracellular K^+ influx.

It is more challenging to compare the absolute and relative hydrostatic pressures obtained here with clinical or experimental measurements. The coupling between electro-chemical and mechanical effects leads to an inherent cascade in which ionic concentration differences induce an osmotic pressure difference across the membrane, transmembrane water flux and cellular swelling, and intracompartmental fluid flow. The difference $p_i - p_e$ between the hydrostatic pressures p_i and p_e is regulated by the intracellular volume changes resulting from transmembrane water movement, modulated by the elastic stiffness K_m of the cell membrane. On the other hand, the absolute value of these hydrostatic pressures are determined by the incompressibility of the fluid environment and the permeability of each compartment. Within this paradigm, our simulations suggest that the ion dynamics can induce localized differences in extracellular hydrostatic pressures of several kPa over a distance of 150 µm, which would correspond to an average spatial gradient of tens of MPa/m. These values are out of range when compared with e.g. the intracranial pressure (ICP), which pulsates with the cardiac and respiratory cycles with (supine) mean ICP values of $\sim$7–15 mmHg relative to baseline atmospheric pressure (1 mmHg = $\sim$133 Pa) in healthy subjects [59, 60], mean ICP wave amplitudes of $\sim$1.5–7 mmHg [61, 62], and spatial differences of less than 1–3 mmHg/m [63, 64]; but more comparable with normal cerebral perfusion pressure (representing the difference between the mean arterial pressure and the ICP) of $50 - 150$ mmHg (6.7 – 20 kPa). In comparison, an osmotic pressure of 1 kPa (7.5 mmHg) across a cellular membrane corresponds to an osmotic concentration difference of only $\sim$0.4 mM. Future modeling work is required to couple e.g. vascular or perivascular pressure pulsations with the interstitial dynamics presented here.

Fluid flow may enhance ion and solute transport by advection in addition to the intrinsically present diffusion. We here discuss the advective contribution to K^+ transport through astrocytic networks. Previous computational studies of spatial K^+ buffering has utilized either models based on cable theory, where contributions from diffusive currents are neglected [65, 66, 67, 68], or applied electrodiffusive frameworks accounting for the coupling of spatiotemporal variations in ion concentrations and electrical potentials [34, 69]. In contrast to the model presented here, neither of these previous models account for cellular swelling and advective transport. We find that K^+ is mainly transported through the ICS, and notably that electrical drift dominates both diffusive and advective transport. Interestingly, we observe a net transport of K^+ away from the input zone even in model scenario M1, where diffusion drives K^+ in the opposite direction (i.e., towards the input zone). The strong dominance of electrical drift in ICS K^+ transport is in accordance with the findings reported in Halnes et al. [34] and Zhu et al. [39]. Further, our findings indicate that osmotically driven flow through the astrocytic syncytium facilitates spatial buffering via advection: our model scenario M3 predicts a 21.5% higher K^+ transport (away from the input zone) than Halnes et al. [34].

Although the exact mechanisms for water transport across astrocytic membranes are debated [3], it is well established that astrocytes have higher water permeability than neurons in part since neurons do not express AQP4 [70]. The high astrocytic water permeability has been hypothesized to stabilize extracellular ion concentrations, shielding neurons from severe swelling [34]. Our findings indeed indicate that cellular swelling, and importantly osmotic transport within the astrocytic network, facilitate in preventing water potential build-up in the ECS and thus neuronal swelling. Further, we find that models for ionic electrodiffusion must account for fluid dynamics and cellular swelling to estimate osmotic pressure across glial-ECS membranes adequately.

The computational model considered here is complex, with numerous model parameters, giving rise to considerable uncertainty. Our sensitivity analysis shows that the maximum superficial fluid velocity varies substantially under variations in a selection of the parameters related to mechanics (compartmental permeability, membrane stiffness, and membrane water permeability). Still, the differences we observe between M1 and M3 are robust to the choice of these model parameters. As such, we deem the current model useful for pointing at a mechanistic understanding of how astrocytic response to neuronal activity may impact fluid movement in the brain.

In order to maintain a reasonable level of complexity, our model distinctly includes electrodiffusion, osmosis, and hydrostatic pressures, while the representation of a number of other mechanisms are substantially simplified. In particular, we let the transmembrane water transport be parameterized by a single transmembrane water permeability (η_{m}), assuming that fluid is carried by passive transporters only. The parameter η_{m} captures the permeability of all (passive) membrane fluid transporters lumped together. However, through which channels fluid flows and in what direction is still an unresolved issue [3] that could be studied further using the here proposed model as a starting point. Furthermore, we have not allowed fluid to enter or leave the system (i.e., closed boundary conditions). A natural next step for this modeling work would be to open up the boundaries to investigate the coupling between brain parenchyma and perivascular spaces. In particular, this approach could be used to study the polarization of AQP4 channels, which are known to be densely packed at the astrocyte endfeet [71].

We conclude that the framework presented here is a promising tool for predicting complex phenomena related to electro-chemical-mechanical interplay in brain tissue. We point at a mechanistic understanding of how astrocytic response to neuronal activity and permeabilities may impact fluid movement in the brain. Our sensitivity analysis supports the idea that reduced glial water permeability may reduce (ICS and) ECS fluid velocities. Further *in-silico* studies with more physiological transmembrane water mechanisms and boundary conditions representing vascular or perivascular pressure pulsations could elucidate open questions related to the role of AQP4 and astrocytes in brain water clearance and homeostasis.

4 Methods

The homogenized tissue is represented by a one-dimensional domain Ω, with length L and outer boundary $\Gamma = \partial\Omega$. We assume that the tissue consists of two compartments representing the ICS (denoted by subscript $r = \mathrm{i}$) and the ECS (denoted by $r = \mathrm{e}$). We predict the evolution in time and distribution in space of the volume fractions α_r, the ion concentrations $[\mathrm{Na}^+]_r$, $[\mathrm{K}^+]_r$, and $[\mathrm{Cl}^-]_r$, the electrical potentials ϕ_r, and the hydrostatic pressures p_r. The model is embedded in the electrodiffusive Kirchhoff-Nernst-Planck framework and builds on previous work on ionic electrodiffusion [34, 38], fluid dynamics [39], and astrocyte modeling [34].

4.1 Governing equations

We consider the following system of coupled, time-dependent, nonlinear partial differential equations. Find the ICS volume fraction $\alpha_\mathrm{i} : \Omega \times (0,T] \to [0,1)$ such that for each $t \in (0,T]$:

$$\frac{\partial \alpha_\mathrm{i}}{\partial t} + \nabla \cdot (\alpha_\mathrm{i} u_\mathrm{i}) = -\gamma_\mathrm{m} w_\mathrm{m}, \tag{1}$$

where $u_\mathrm{i} : \Omega \times (0,T] \to \mathbb{R}$ (m/s) is the ICS fluid velocity field. The transmembrane water flux w_m is driven by osmotic and hydrostatic pressure, and will be discussed further in Section 4.3. The coefficient γ_m (1/m) represents the area of cell membrane per unit volume of tissue. By definition, the total volume fractions sum to 1, and we assume that neurons occupy 40 % of the total tissue volume [34, 72]. We thus have that:

$$\alpha_\mathrm{e} = (1 - 0.4) - \alpha_\mathrm{i}. \tag{2}$$

Further, for each ion species $k \in \{\mathrm{Na}^+, \mathrm{K}^+, \mathrm{Cl}^-\}$ and for $r = \{\mathrm{i}, \mathrm{e}\}$, find the ion concentration $[k]_r : \Omega \times (0,T] \to \mathbb{R}$ and the electrical potential $\phi_r : \Omega \times (0,T] \to \mathbb{R}$ such that for each $t \in (0,T]$:

$$\frac{\partial (\alpha_\mathrm{i}[k]_\mathrm{i})}{\partial t} + \nabla \cdot (\alpha_\mathrm{i} j^k_\mathrm{i}) = -\gamma_\mathrm{m} j^k_\mathrm{m}, \tag{3a}$$

$$\frac{\partial (\alpha_\mathrm{e}[k]_\mathrm{e})}{\partial t} + \nabla \cdot (\alpha_\mathrm{e} j^k_\mathrm{e}) = \gamma_\mathrm{m} (j^k_\mathrm{m} + j^k_\mathrm{input} + j^k_\mathrm{decay}), \tag{3b}$$

where $j_{\mathrm{i}}^k = j_{\mathrm{i}}^k(x,t)$ and $j_{\mathrm{e}}^k = j_{\mathrm{e}}^k(x,t)$ (mol/(m^{2}s)) are the compartmental ionic flux densities for each ion species k. Modeling of the transmembrane ion flux density j_{m}^k, the input ion flux density j_{input}^k, and the decay ion flux density j_{decay}^k will be discussed further in Sections 4.4–4.5. Note that (3) follows from first principles and express conservation of ion concentrations in each region. Moreover, we assume that the ion flux densities satisfy:

$$-\sum_k z_k \nabla \cdot (\alpha_{\mathrm{i}} j_{\mathrm{i}}^k) - \gamma_{\mathrm{m}} \sum_k z_k j_{\mathrm{m}}^k = 0, \tag{4a}$$

$$-\sum_k z_k \nabla \cdot (\alpha_{\mathrm{e}} j_{\mathrm{e}}^k) + \gamma_{\mathrm{m}} \sum_k z_k j_{\mathrm{m}}^k = 0, \tag{4b}$$

where z_k (unitless) is the valence of ion species k. Note that (4) arises from assuming electroneutrality, i.e., that the sum of all charge inside a compartment is zero. Given the smallness of the capacitance and that we do not model action potentials, this is a well-established approximation to use in place of the charge-capacitor relation that is commonly used when modeling electrodiffusion [38]. We further assume that the compartmental ionic flux densities $j_r^k : \Omega \times (0,T] \to \mathbb{R}$ are driven by diffusion, electric drift, and advection:

$$j_r^k = -\frac{D_k}{\lambda_r^2} \nabla [k]_r - \frac{D_k z_k}{\lambda_r^2 \psi} [k]_r \nabla \phi_r + u_r [k]_r, \quad r = \mathrm{i}, \mathrm{e}. \tag{5}$$

Here, D_k (m^2/s) denotes the diffusion coefficient of ion species k and λ_r (unitless) denotes the tortuosity of compartment r. The constant $\psi = RT/F$ combines Faraday's constant F (C/mol), the absolute temperature T (K), and the gas constant R (J/(molK)).

We now turn to the dynamics of the fluid velocity fields u_r and the hydrostatic pressures $p_r : \Omega \times (0,T] \to \mathbb{R}$ (Pa). We will consider three different models (M1, M2, and M3) for the compartmental fluid velocities u_i and u_e that are detailed in Section 4.2. The relation between the intra- and extracellular hydrostatic pressure p_{i} and p_{e} is given by the force balance on the membrane [39, 38]:

$$p_{\mathrm{i}} - p_{\mathrm{e}} = K_{\mathrm{m}}(\alpha_{\mathrm{i}} - \alpha_{\mathrm{i,init}}) + p_{\mathrm{m,init}}, \tag{6}$$

where K_{m} (Pa) denotes the membrane stiffness, $\alpha_{\mathrm{i,init}}$ (unitless) denotes the initial intracellular volume fraction, and $p_{\mathrm{m,init}}$ (Pa) is the initial hydrostatic pressure difference across the membrane (see Table 2). Furthermore, we assume that the volume–fraction weighted fluid velocity is divergence free; that is:

$$\nabla \cdot \left(\sum_r \alpha_r u_r \right) = 0. \tag{7}$$

By inserting (6) and the relevant expressions for the compartmental fluid velocities u_i and u_e (see Section 4.2 for further details) into (7), we obtain an equation for the extracellular hydrostatic pressure.

The combination of (1), (3), (4), and (7) with insertion of (5) and (6), and the expressions for u_r (c.f. Section 4.2) define a system of 10 differential equations for the 10 unknown fields (α_i, $[k]_r$, ϕ_r, and p_e). Note that the extracellular volume fraction α_e and the intracellular hydrostatic pressure p_i can be calculated using respectively (2) and (6). Appropriate initial conditions, boundary conditions, and importantly membrane mechanisms close the system.

4.2 Expressions for fluid velocities (model scenarios M1, M2, and M3)

To model compartmental fluid flow, we consider three different modeling setups:

M1 We assume that the compartmental fluid flow is driven by hydrostatic pressure gradients. Specifically, the fluid velocities are given by:

$$u_\mathrm{i} = -\kappa_\mathrm{i} \nabla p_\mathrm{i}, \tag{8a}$$

$$u_\mathrm{e} = -\kappa_\mathrm{e} \nabla p_\mathrm{e}, \tag{8b}$$

where κ_r ($\mathrm{m}^2/(\mathrm{Pa\ s})$) denotes the mobility of compartment r. We will refer to κ_r as the compartmental permeability.

M2 We assume that fluid flow in the glial network is driven by hydrostatic and osmotic pressure gradients. Since Na^+, K^+, and Cl^- can move through the ICS via gap junctions, we assume that they do not contribute to osmosis. Thus, only the immobile ions drive the osmotic flow. As osmotic forces only act across membranes, we assume that fluid flow in the ECS is only driven by hydrostatic pressure gradients. The fluid velocities are given by:

$$u_\mathrm{i} = -\kappa_\mathrm{i}(\nabla p_\mathrm{i} - iRT \nabla \frac{a_\mathrm{i}}{\alpha_\mathrm{i}}), \tag{9a}$$

$$u_\mathrm{e} = -\kappa_\mathrm{e} \nabla p_\mathrm{e}, \tag{9b}$$

where i (unitless) is the Van't Hoff factor, and a_i ($\mathrm{mol}/\mathrm{m}^3$) is the concentration of immobile ions.

M3 We follow Zhu et al. 2021 [39] and assume that the intracellular fluid flow is driven by hydrostatic and osmotic forces, while the extracellular fluid flow is driven by hydrostatic and electro-osmotic forces. To model the electro-osmotic flow, we use the Helmholtz-Smoluchowski approximation[41]. The fluid velocities are given by:

$$u_\mathrm{i} = -\kappa_\mathrm{i}(\nabla p_\mathrm{i} - iRT \nabla \frac{a_\mathrm{i}}{\alpha_\mathrm{i}}), \tag{10a}$$

$$u_\mathrm{e} = -\kappa_\mathrm{e} \nabla p_\mathrm{e} - \frac{\varepsilon_r \varepsilon_0 \zeta}{\mu} \nabla \phi_\mathrm{e}. \tag{10b}$$

Here, ε_r (unitless) is the relative permittivity of the extracellular solution, ε_0 (F/m) is the vacuum permittivity, ζ (V) is the zeta-potential, and μ (Pas) is the viscosity of water .

4.3 Transmembrane fluid flow

The transmembrane fluid flow is driven by hydrostatic and osmotic pressure gradients, and the fluid velocity, w_m (m/s), is expressed as:

$$w_\mathrm{m} = \eta_\mathrm{m}(p_\mathrm{i} - p_\mathrm{e} + iRT(O_\mathrm{e} - O_\mathrm{i})). \tag{11}$$

Here, η_m (m/(Pas)) is the membrane water permeability and O_r is the osmolarity of compartment r. We assume that all ion species contribute to the osmolarity, which is given by

$$O_r = \frac{a_r}{\alpha_r} + \sum_k [k]_r. \tag{12}$$

Multiplying O_r by $-iRT$ gives us the solute potential in compartment r, Π_r.

4.4 Membrane mechanisms

We adopt the ionic membrane mechanisms from Halnes et al. 2013 [34]. The mechanisms include a Na^+ leak channel, a Cl^- leak channel, an inward-rectifying K^+ channel, and a Na^+/K^+ pump. The membrane flux densities (mol/(m^2s)) are given by:

$$j_\mathrm{m}^\mathrm{Na} = \frac{\bar{g}_\mathrm{Na}}{F z_\mathrm{Na}}(\phi_\mathrm{m} - E_\mathrm{Na}) + 3 j_\mathrm{pump}, \tag{13a}$$

$$j_\mathrm{m}^\mathrm{K} = \frac{\bar{g}_\mathrm{K} f_\mathrm{Kir}}{F z_\mathrm{K}}(\phi_\mathrm{m} - E_\mathrm{K}) - 2 j_\mathrm{pump}, \tag{13b}$$

$$j_\mathrm{m}^\mathrm{K} = \frac{\bar{g}_\mathrm{Cl}}{F z_\mathrm{Cl}}(\phi_\mathrm{m} - E_\mathrm{Cl}), \tag{13c}$$

where $\bar{g}_k$ (S/m^2) is the membrane conductance for ion species k, ϕ_m (V) is the membrane potential (defined as $\phi_\mathrm{i} - \phi_\mathrm{e}$), and E_k (V) is the reversal potential. The reversal potentials are given by the Nernst equation:

$$E_k = \frac{RT}{F z_k} \ln\left(\frac{[k]_\mathrm{e}}{[k]_\mathrm{i}}\right). \tag{14}$$

Further, the Kir-function, f_Kir, which modifies the inward-rectifying K^+ current, is given by:

$$f_\mathrm{Kir}([\mathrm{K}^+]_\mathrm{e}, \Delta\phi, \phi_\mathrm{m}) = \sqrt{\frac{[\mathrm{K}^+]_\mathrm{e}}{[\mathrm{K}^+]_\mathrm{e,init}}} \left[\frac{AB}{CD}\right],$$

where

$$A = 1 + \exp(18.4/42.4), \qquad B = 1 + \exp(-(0.1186 + E_\mathrm{K,init})/0.0441),$$

$$C = 1 + \exp((\Delta\phi + 0.0185)/0.0425), \quad D = 1 + \exp(-(0.1186 + \phi_\mathrm{m})/0.0441).$$

Here, $\Delta\phi = \phi_m - E_k$, and $E_{K,init}$ is the reversal potential for K^+ at initial ion concentrations. Finally, the pump flux density ($mol/(m^2 s)$) is given by:

$$j_{pump} = \rho_{pump} \left(\frac{[Na^+]_i^{1.5}}{[Na^+]_i^{1.5} + P_{Nai}^{1.5}} \right) \left(\frac{[K^+]_e}{[K^+]_e + P_{Ke}} \right), \tag{15}$$

where ρ_{pump} ($mol/(m^2 s)$) is the maximum pump rate, P_{Nai} (mol/m^3) is the $[Na^+]_i$ threshold, and P_{Ke} (mol/m^3) is the $[K^+]_e$ threshold.

4.5 Input/decay fluxes

To stimulate the system, we follow the same procedure as in Halnes et al. 2013 [34]. We assume that there is a group of highly active neurons within the input zone, defined to be the interval $[L_1, L_2]$ with $L_1 = 1.35 \cdot 10^{-4}$ m and $L_2 = 1.65 \cdot 10^{-4}$ m, during the time interval $[10\,s, 210\,s]$. The neurons are not modeled explicitly, but we mimic their activity by injecting a constant K^+ current into the ECS and removing the same amount of Na^+ ions simultaneously. The input current $j^k_{input} : [L_1, L_2] \times [10\,s, 210\,s] \to \mathbb{R}$ is given by:

$$j^K_{input} = -j^{Na}_{input} = j_{in}, \tag{16}$$

where j_{in} ($mol/(m^2 s)$) is constant. We set the strength of j_{in} (see Table 2) such that the extracellular K^+ concentration in the input zone reaches a maximum value of approximately 10 mM during the simulations. At this concentration level, we expect the K^+ buffering process to play a critical role; still, the concentration is below the level we observe in pathological conditions such as spreading depression (see Halnes et al. [34] and references therein).

To mimic neuronal pumps and cotransporters, we remove K^+ ions from the extracellular space at a given decay rate and add the same amount of Na^+ ions. The decay is proportional to the extracellular K^+ concentration and defined across the whole domain. Specifically, the decay current $j^k_{decay} : \Omega \times (0, T] \to \mathbb{R}$ ($mol/(m^2 s)$) is given by:

$$j^K_{decay} = -j^{Na}_{decay} = -k_{dec}([K^+]_e - [K^+]_{e,init}), \tag{17}$$

where k_{dec} denotes the $[K^+]_e$ decay factor, and $[K^+]_{e,init}$ the initial extracellular K^+ concentration.

4.6 Model parameters

All parameters of the system are as listed in Table 2.

4.6.1 Choice of membrane stiffness

Lu et al. 2006 [73, Figure 1D, Figure S6] report the Young's modulus E of individual astrocytes in the hippocampus for different deformation frequencies with $E \approx 300$ Pa for 30 Hz, $E \approx 420$ Pa for 100 Hz, and $E \approx 520$ Pa for 200 Hz, and a Poisson's ratio

Table 2. Model parameters

Symbol	Definition	Value	Ref.
L	Length of domain	$3.0 \cdot 10^{-4}$ m	[34]
F	Faraday's constant	96485.3 C/mol	
R	Gas constant	8.314 J/(molK)	
T	Temperature	310.15 K	
i	Van't Hoff factor	1	
D_{Na}	Na^+ diffusion constant	$1.33 \cdot 10^{-9}$ m^2/s	[34]
D_{K}	K^+ diffusion constant	$1.96 \cdot 10^{-9}$ m^2/s	[34]
D_{Cl}	Cl^- diffusion constant	$2.03 \cdot 10^{-9}$ m^2/s	[34]
λ_{i}	Intracellular tortuosity	3.2	[34]
λ_{e}	Extracellular tortuosity	1.6	[34]
γ_{m}	Membrane area per unit volume of tissue	$8 \cdot 10^6$ 1/m	[34]
$\bar{g}_{\mathrm{Na}}$	Membrane conductance for Na^+	1 S/m^2	[34]
$\bar{g}_{\mathrm{K}}$	Membrane conductance for K^+	16.96 S/m^2	[34]
$\bar{g}_{\mathrm{Cl}}$	Membrane conductance for Cl^-	0.5 S/m^2	[34]
ρ_{pump}	Maximum pump rate	$1.12 \cdot 10^{-6}$ mol/(m^{2}s)	[34]
P_{Nai}	$[Na^+]_{\mathrm{i}}$ threshold for Na^+/K^+ pump	10 mol/m^3	[34]
P_{Ke}	$[K^+]_{\mathrm{e}}$ threshold for Na^+/K^+ pump	1.5 mol/m^3	[34]
η_{m}	Membrane water permeability	$8.14 \cdot 10^{-14}$ m/(Pas)	[35]
K_{m}	Membrane stiffness	$2.294 \cdot 10^3$ Pa	[73]
κ_{i}	ICS permeability	$1.8375 \cdot 10^{-14}$ m^2/(Pas)	
κ_{e}	ECS permeability	$1.8375 \cdot 10^{-14}$ m^2/(Pas)	[27]
ε_{r}	Relative permittivity of the ECS	84.6	[41]
ε_0	Vacuum permittivity	$8.85 \cdot 10^{-12}$ F/m	[41]
ζ	Zeta-potential	$-22.8 \cdot 10^{-3}$ V	[41]
μ	Viscosity of water	$6.4 \cdot 10^{-4}$ Pa s	[41]
$p_{\mathrm{m,init}}$	Initial transmembrane hydrostatic pressure difference	$1 \cdot 10^3$ Pa	[74]
$j_{\mathrm{in}}^{\mathrm{M0}}$	Constant input flux density (M0)	$8.28 \cdot 10^{-7}$ mol/(m^{2}s)	
$j_{\mathrm{in}}^{\mathrm{M1}}$	Constant input flux density (M1)	$8.0 \cdot 10^{-7}$ mol/(m^{2}s)	
$j_{\mathrm{in}}^{\mathrm{M2}}$	Constant input flux density (M2)	$9.15 \cdot 10^{-7}$ mol/(m^{2}s)	
$j_{\mathrm{in}}^{\mathrm{M3}}$	Constant input flux density (M3)	$9.05 \cdot 10^{-7}$ mol/(m^{2}s)	
k_{dec}	Decay factor for $[K^+]_{\mathrm{e}}$	$2.9 \cdot 10^{-8}$ m/s	[34]

$\nu = 0.47$. We use the mean Young's modulus (413 Pa) to calculate the bulk modulus (stiffness constant) K_{m} as:

$$K_{\mathrm{m}} = \frac{E}{3(1-2\nu)} = 2.294 \cdot 10^3 \,\mathrm{Pa}.$$

4.7 Boundary conditions

We apply sealed-end boundary conditions to the system, that is, no ions and no fluid are allowed to enter or leave the system on the boundary Γ:

$$\alpha_r j_r^k \cdot n_\Gamma = 0 \quad \text{on } \Gamma, \tag{18a}$$

$$\alpha_r u_r \cdot n_\Gamma = 0 \quad \text{on } \Gamma, \tag{18b}$$

where n_Γ is the outward pointing normal vector.

The extracellular electrical potential, ϕ_e, and the extracellular hydrostatic pressure, p_e, are only determined up to constants. To constrain the electrical potential, we require that:

$$\int_\Omega \phi_e dx = 0. \tag{19}$$

We enforce this zero-average constraint by introducing an additional unknown (a Lagrange multiplier) c_e. For the extracellular hydrostatic pressure, we set

$$p_e = 0 \quad \text{on } \Gamma_{\text{right}}. \tag{20}$$

4.8 Initial conditions

We obtain initial conditions for the system through a two-step procedure. First, we specify a set of pre-calibrated initial values (Table 3a, Pre-calibrated column). Second, we calibrate the model by running a simulation for $1 \cdot 10^6$ s. For the calibration, we set the transmembrane water permeability to zero and use $N = 100$ and $\Delta t = 10^{-2}$. The final values from the calibration are listed in Table 3a (Post-calibrated column).

Table 3. Initial conditions and baseline values. * Values with more significant digits included were used in the simulations. (Available with the source code.)

Variable	Pre-calibrated	Post-calibrated*	Ref.
α_i	0.4	0.4	[34]
$[Na^+]_i$	15.189 mM	15.475 mM	[34]
$[Na^+]_e$	144.662 mM	144.091 mM	[34]
$[K^+]_i$	99.959 mM	99.892 mM	[34]
$[K^+]_e$	3.082 mM	3.216 mM	[34]
$[Cl^-]_i$	5.145 mM	5.364 mM	[34]
$[Cl^-]_e$	133.71 mM	133.273 mM	[34]

(a) Initial conditions.

Variable	Value	Eq.
α_e	0.2	2
ϕ_m	-85.9 mV	4
p_i	$1 \cdot 10^3$ Pa	6
p_e	0.0 Pa	7

(b) Baseline values derived from the state variables.

To ensure fluid equilibrium at $t = 0$ s and electroneutrality of the system, we define a set of immobile macromolecules, a_i and a_e (mol/m^3), with charge number z_0 (unitless) based on the initial ion concentrations. These are defined as constant concentrations with respect to the total volume of the system. Requiring an electroneutral system and zero transmembrane fluid

flux at $t = 0\,\mathrm{s}$ gives:

$$F\left(\sum_k z_k[k]_{\mathrm{e,init}} + z_0\frac{a_\mathrm{e}}{\alpha_{\mathrm{e,init}}}\right) = 0, \tag{21a}$$

$$F\left(\sum_k z_k[k]_{\mathrm{i,init}} + z_0\frac{a_\mathrm{i}}{\alpha_{\mathrm{i,init}}}\right) = 0, \tag{21b}$$

$$\eta_\mathrm{m}\left(p_{\mathrm{m,init}} + RT\left(\frac{a_\mathrm{e}}{\alpha_{\mathrm{e,init}}} + \sum_k [k]_{\mathrm{e,init}} - \frac{a_\mathrm{i}}{\alpha_{\mathrm{i,init}}} - \sum_k [k]_{\mathrm{i,init}}\right)\right) = 0. \tag{21c}$$

Solving (21) gives the following expressions for z_0, a_i, and a_e:

$$z_0 = \frac{\sum_k z_k[k]_{\mathrm{e,init}} - \sum_k z_k[k]_{\mathrm{i,init}}}{\frac{p_{\mathrm{m,init}}}{RT} + \sum_k [k]_{\mathrm{e,init}} - \sum_k [k]_{\mathrm{i,init}}}, \tag{22a}$$

$$a_\mathrm{i} = -\sum_k z_k[k]_{\mathrm{i,init}}\frac{\alpha_{\mathrm{i,init}}}{z_0}, \tag{22b}$$

$$a_\mathrm{e} = -\sum_k z_k[k]_{\mathrm{e,init}}\frac{\alpha_{\mathrm{e,init}}}{z_0}. \tag{22c}$$

To ensure strict electroneutrality and fluid equilibrium, we calculate the values at the beginning of each simulation. By using the post-calibrated initial conditions listed in Table 3, the values are approx. $z_0 = -0.6$, $a_\mathrm{e} = 4.7\,\mathrm{mM}$, and $a_\mathrm{i} = 73.5\,\mathrm{mM}$. Note that z_0 is interpreted as the average charge number of the macromolecules, and may thus be a decimal number (e.g., if not all the immobile macromolecules added to the system are charged).

4.9 Numerical implementation and verification

We discretize the system using a finite element method in space with characteristic mesh size Δx and a first order implicit finite difference scheme in time with time step Δt. Our numerical scheme and implementation builds on previous work presented in Ellingsrud et al. 2021 [40].

The numerical scheme is implemented via the FEniCS finite element library [75] (Python 3.8), and the code is openly available at https://github.com/martejulie/fluid-flow-in-astrocyte-networks. To determine the time step Δt and the mesh size Δx, we perform a numerical convergence study. Specifically, we apply the numerical scheme outlined above for model scenario M1 for different mesh resolutions and time steps: $\Delta x = L/N$ for $N = 25, 50, 100, 200, 400, 800$ and $\Delta t = 1, 10^{-1}, 10^{-2}, 10^{-3}, 10^{-4}$ s. For each simulation, we calculate the peak extracellular superficial fluid velocity and the peak concentration of ECS K^+ at $t = 20\,\mathrm{s}$. We find that the peak extracellular superficial fluid velocity and the ECS K^+ concentration converge towards $0.271\,\mu\mathrm{m/min}$ and $9.186\,\mathrm{mM}$, respectively, as the temporal and spatial resolution increase (Table 4a,b). Based on our findings, we choose $\Delta t = 10^{-3}\mathrm{s}$ and $N = 400$ for all simulations presented within this work.

Table 4. Numerical verification: quantities of interest converge under spatial and temporal discrete refinement.

Δt \ N	25	50	100	200	400	800
1	0.217	0.268	0.269	0.271	0.272	0.272
10^{-1}	0.216	0.267	0.268	0.270	0.270	0.271
10^{-2}	0.216	0.267	0.268	0.271	0.271	0.271
10^{-3}	0.216	0.267	0.268	0.271	0.271	0.271
10^{-4}	0.216	0.267	0.268	0.271	0.271	0.271

(a) $\max(\alpha_e u_e)$ (μm/min)

Δt \ N	25	50	100	200	400	800
1	7.799	9.204	9.198	9.205	9.208	9.207
10^{-1}	7.774	9.174	9.169	9.175	9.177	9.177
10^{-2}	7.780	9.182	9.176	9.183	9.185	9.185
10^{-3}	7.781	9.183	9.177	9.184	9.186	9.186
10^{-4}	7.781	9.183	9.177	9.184	9.186	9.186

(b) $\max([K^+]_e)$ (mM)

4.10 Calculation of advection/diffusion and advection/drift fractions

We calculate the advection/diffusion fraction F_{diff} and the advection/electric-drift fraction F_{drift} for ion species k as follows:

$$F^k_{\text{diff}} = |j^k_{\text{adv}}/j^k_{\text{diff}}|, \tag{23}$$

$$F^k_{\text{drift}} = |j^k_{\text{adv}}/j^k_{\text{drift}}|, \tag{24}$$

where j^k_{adv} (mol/(m^{2}s)), j^k_{diff} (mol/(m^{2}s)), and j^k_{drift} (mol/(m^{2}s)) are the advective, diffusive, and electric-drift components of the peak total ionic flux at $t = 200$ s, respectively.

5 Acknowledgements

We want to thank Yoichiro Mori for valuable discussions and Jørgen S. Dokken for help with setting up the GitHub repositories.

This project has received funding from the European Research Council (ERC) under the European Union's Horizon 2020 research and innovation programme under grant agreement 714892. In addition, AJE and MER acknowledges support and funding from the Research Council of Norway (RCN) via FRIPRO grant agreement #324239 (EMIx).

References

1. Fultz NE, Bonmassar G, Setsompop K, Stickgold RA, Rosen BR, Polimeni JR, et al. Coupled electrophysiological, hemodynamic, and cerebrospinal fluid oscillations in human sleep. Science. 2019;366(6465):628–631.

2. Rasmussen R, O'Donnell J, Ding F, Nedergaard M. Interstitial ions: A key regulator of state-dependent neural activity? Prog Neurobiol. 2020;193:101802.

3. MacAulay N. Molecular mechanisms of brain water transport. Nat Rev Neurosci. 2021;22(6):326–344.

4. Mestre H, Du T, Sweeney AM, Liu G, Samson AJ, Peng W, et al. Cerebrospinal fluid influx drives acute ischemic tissue swelling. Science. 2020;367(6483):eaax7171.

5. Bakker EN, Bacskai BJ, Arbel-Ornath M, Aldea R, Bedussi B, Morris AW, et al. Lymphatic clearance of the brain: perivascular, paravascular and significance for neurodegenerative diseases. Cell Mol Neurobiol. 2016;36:181–194.

6. Nedergaard M, Goldman SA. Glymphatic failure as a final common pathway to dementia. Science. 2020;370(6512):50–56.

7. LaMontagne E, Muotri AR, Engler AJ. Recent advancements and future requirements in vascularization of cortical organoids. Front Bioeng Biotechnol. 2022;10:2059.

8. Aitken P, Somjen G. The sources of extracellular potassium accumulation in the CA1 region of hippocampal slices. Brain Res. 1986;369(1-2):163–167.

9. Nicholson C, Ten Bruggencate G, Stockle H, Steinberg R. Calcium and potassium changes in extracellular microenvironment of cat cerebellar cortex. J Neurophysiol. 1978;41(4):1026–1039.

10. Utzschneider D, Kocsis J, Devor M. Mutual excitation among dorsal root ganglion neurons in the rat. Neurosci Lett. 1992;146(1):53–56.

11. Stokum JA, Kwon MS, Woo SK, Tsymbalyuk O, Vennekens R, Gerzanich V, et al. SUR1-TRPM4 and AQP4 form a heteromultimeric complex that amplifies ion/water osmotic coupling and drives astrocyte swelling. Glia. 2018;66(1):108–125.

12. Tait MJ, Saadoun S, Bell BA, Papadopoulos MC. Water movements in the brain: role of aquaporins. Trends Neurosci. 2008;31(1):37–43.

13. Xu ZY, Liu HD, Lau LT, Yingge Z, Zhao R, Tong GL, et al. Responses of astrocyte to simultaneous glutamate and arachidonic acid treatment. Neurochem Int. 2009;55(1-3):143–150.

14. Arizono M, Inavalli VK, Bancelin S, Fernández-Monreal M, Nägerl UV. Super-resolution shadow imaging reveals local remodeling of astrocytic microstructures and brain extracellular space after osmotic challenge. Glia. 2021;69(6):1605–1613.

15. Iliff JJ, Wang M, Liao Y, Plogg BA, Peng W, Gundersen GA, et al. A paravascular pathway facilitates CSF flow through the brain parenchyma and the clearance of interstitial solutes, including amyloid β. Sci Transl Med. 2012;4(147):147ra111–147ra111.

16. Kelley DH, Bohr T, Hjorth PG, Holst SC, Hrabětová S, Kiviniemi V, et al. The glymphatic system: Current understanding and modeling. iScience. 2022;25(9):104987.

17. Larsen BR, MacAulay N. Activity-dependent astrocyte swelling is mediated by pH-regulating mechanisms. Glia. 2017;65(10):1668–1681.

18. Mestre H, Hablitz LM, Xavier AL, Feng W, Zou W, Pu T, et al. Aquaporin-4-dependent glymphatic solute transport in the rodent brain. Elife. 2018;7:e40070.

19. Salman MM, Kitchen P, Iliff JJ, Bill RM. Aquaporin 4 and glymphatic flow have central roles in brain fluid homeostasis. Nat Rev Neurosci. 2021;22(10):650–651.

20. Szczygielski J, Kopańska M, Wysocka A, Oertel J. Cerebral microcirculation, perivascular unit, and glymphatic system: role of aquaporin-4 as the gatekeeper for water homeostasis. Front Neurol. 2021;12:2270.

21. Carnevale NT, Hines ML. The NEURON book. Cambridge University Press; 2006.

22. Newton AJ, McDougal RA, Hines ML, Lytton WW. Using NEURON for reaction-diffusion modeling of extracellular dynamics. Front Neuroinform. 2018;12:41.

23. Gupta S, Czech J, Kuczewski R, Bartol TM, Sejnowski TJ, Lee RE, et al. Spatial stochastic modeling with MCell and CellBlender. arXiv preprint arXiv:181000499. 2018;.

24. Bell M, Bartol T, Sejnowski T, Rangamani P. Dendritic spine geometry and spine apparatus organization govern the spatiotemporal dynamics of calcium. J Gen Physiol. 2019;151(8):1017–1034.

25. Daversin-Catty C, Vinje V, Mardal KA, Rognes ME. The mechanisms behind perivascular fluid flow. PLoS One. 2020;15(12):e0244442.

26. Kedarasetti RT, Drew PJ, Costanzo F. Arterial pulsations drive oscillatory flow of CSF but not directional pumping. Sci Rep. 2020;10(1):10102.

27. Holter KE, Kehlet B, Devor A, Sejnowski TJ, Dale AM, Omholt SW, et al. Interstitial solute transport in 3D reconstructed neuropil occurs by diffusion rather than bulk flow. Proc Natl Acad Sci. 2017;114(37):9894–9899.

28. Ray L, Iliff JJ, Heys JJ. Analysis of convective and diffusive transport in the brain interstitium. Fluids Barriers CNS. 2019;16(1):1–18.

29. Kedarasetti RT, Drew PJ, Costanzo F. Arterial vasodilation drives convective fluid flow in the brain: a poroelastic model. Fluids Barriers CNS. 2022;19(1):1–24.

30. Jin BJ, Smith AJ, Verkman AS. Spatial model of convective solute transport in brain extracellular space does not support a "glymphatic" mechanism. J Gen Physiol. 2016;148(6):489–501.

31. Croci M, Vinje V, Rognes ME. Uncertainty quantification of parenchymal tracer distribution using random diffusion and convective velocity fields. Fluids Barriers CNS. 2019;16:1–21.

32. Vinje V, Zapf B, Ringstad G, Eide PK, Rognes ME, Mardal K. Human brain solute transport quantified by glymphatic MRI-informed biophysics during sleep and sleep deprivation. bioRxiv. 2023; p. 2023–01.

33. Ray LA, Pike M, Simon M, Iliff JJ, Heys JJ. Quantitative analysis of macroscopic solute transport in the murine brain. Fluids Barriers CNS. 2021;18(1):1–19.

34. Halnes G, Østby I, Pettersen KH, Omholt SW, Einevoll GT. Electrodiffusive model for astrocytic and neuronal ion concentration dynamics. PLoS Comput Biol. 2013;9(12):e1003386.

35. Østby I, Øyehaug L, Einevoll GT, Nagelhus EA, Plahte E, Zeuthen T, et al. Astrocytic mechanisms explaining neural-activity-induced shrinkage of extraneuronal space. PLoS Computat Biol. 2009;5(1):e1000272.

36. Jin BJ, Zhang H, Binder DK, Verkman A. Aquaporin-4–dependent K^+ and water transport modeled in brain extracellular space following neuroexcitation. J Gen Physiol. 2013;141(1):119–132.

37. Asgari M, De Zélicourt D, Kurtcuoglu V. How astrocyte networks may contribute to cerebral metabolite clearance. Sci Rep. 2015;5(1):1–13.

38. Mori Y. A multidomain model for ionic electrodiffusion and osmosis with an application to cortical spreading depression. Physica D. 2015;308:94–108.

39. Zhu Y, Xu S, Eisenberg RS, Huang H. Optic nerve microcirculation: Fluid flow and electrodiffusion. Phys Fluids. 2021;33(4):041906.

40. Ellingsrud AJ, Boullé N, Farrell PE, Rognes ME. Accurate numerical simulation of electrodiffusion and water movement in brain tissue. Math Med Biol. 2021;38(4):516–551.

41. Wang T, Kleiven S, Li X. Electroosmosis based novel treatment approach for cerebral edema. IEEE Trans Biomed Eng. 2020;68(9):2645–2653.

42. Ransom B, Yamate C, Connors B. Activity-dependent shrinkage of extracellular space in rat optic nerve: a developmental study. J Neurosci. 1985;5:532–535.

43. Walz W, Hinks E. Carrier-mediated KCl accumulation accompanied by water movements is involved in the control of physiological K^+ levels by astrocytes. Brain Res. 1985;343:44–51.

44. Amiry-Moghaddam M, Frydenlund D, Ottersen O. Anchoring of aquaporin-4 in brain: Molecular mechanisms and implications for the physiology and pathophysiology of water transport. Neuroscience. 2004;129:999–1010.

45. Nagelhus E, Mathiisen T, Ottersen O. Aquaporin-4 in the central nervous system: cellular and subcellular distribution and coexpression with Kir4.1. Neuroscience. 2004;129(4):905–913.

46. Halnes G, Pettersen KH, Øyehaug L, Rognes ME, Einevoll GT. Astrocytic ion dynamics: Implications for potassium buffering and liquid flow. In: Computational Glioscience. Springer; 2019. p. 363–391.

47. Halnes G, Mäki-Marttunen T, Keller D, Pettersen KH, Andreassen OA, Einevoll GT. Effect of ionic diffusion on extracellular potentials in neural tissue. PLoS Comput Biol. 2016;12(11):e1005193.

48. Sætra MJ, Einevoll GT, Halnes G. An electrodiffusive neuron-extracellular-glia model with somatodendritic interactions. bioRxiv. 2020; p. 2020–07.

49. Walz W, Hertz L. Intracellular ion changes of astrocytes in response to extracellular potassium. J Neurosci Res. 1983;10(4):411–423.

50. Dietzel I, Heinemann U, Hofmeier G, Lux H. Stimulus-induced changes in extracellular Na^+ and Cl^- concentration in relation to changes in the size of the extracellular space. Exp Brain Res. 1982;46:73–84.

51. Grisar T. Glial and neuronal Na^+-K^+ pump in epilepsy. Ann Neurol. 1984;16(S1):S128–S134.

52. Cserr H, Cooper D, Suri P, Patlak C. Efflux of radiolabeled polyethylene glycols and albumin from rat brain. Am J Physiol Renal Physiol. 1981;240(4):F319–F328.

53. Bradbury M, Cserr H, Westrop R. Drainage of cerebral interstitial fluid into deep cervical lymph of the rabbit. Am J Physiol Renal Physiol. 1981;240(4):F329–F336.

54. Szentistvanyi I, Patlak CS, Ellis RA, Cserr HF. Drainage of interstitial fluid from different regions of rat brain. Am J Physiol Renal Physiol. 1984;246(6):F835–F844.

55. Rosenberg G, Kyner W, Estrada E. Bulk flow of brain interstitial fluid under normal and hyperosmolar conditions. Am J Physiol Renal Physiol. 1980;238(1):F42–F49.

56. Abbott NJ, Bundgaard M, Cserr HF. Tightness of the blood-brain barrier and evidence for brain interstitial fluid flow in the cuttlefish, Sepia officinalis. J Physiol. 1985;368(1):213–226.

57. Nicholson C. Diffusion and related transport mechanisms in brain tissue. Rep Prog Phys. 2001;64(7):815.

58. Ray LA, Pike M, Simon M, Iliff JJ, Heys JJ. Quantitative analysis of macroscopic solute transport in the murine brain. Fluids Barriers CNS. 2021;18(1):1–19.

59. Liu S, Tao R, Wang M, Tian J, Genin GM, Lu TJ, et al. Regulation of cell behavior by hydrostatic pressure. Appl Mech Rev. 2019;71(4).

60. Albeck MJ, Børgesen SE, Gjerris F, Schmidt JF, Sørensen PS. Intracranial pressure and cerebrospinal fluid outflow conductance in healthy subjects. J Neurosurg. 1991;74(4):597–600.

61. Eide PK. Comparison of simultaneous continuous intracranial pressure (ICP) signals from ICP sensors placed within the brain parenchyma and the epidural space. Med Eng Phys. 2008;30(1):34–40.

62. Wagshul ME, Eide PK, Madsen JR. The pulsating brain: a review of experimental and clinical studies of intracranial pulsatility. Fluids Barriers CNS. 2011;8(1):1–23.

63. Eide PK, Sæhle T. Is ventriculomegaly in idiopathic normal pressure hydrocephalus associated with a transmantle gradient in pulsatile intracranial pressure? Acta Neurochir. 2010;152:989–995.

64. Vinje V, Ringstad G, Lindstrøm EK, Valnes LM, Rognes ME, Eide PK, et al. Respiratory influence on cerebrospinal fluid flow – a computational study based on long-term intracranial pressure measurements. Sci Rep. 2019;9(1):9732.

65. Gardner-Medwin A. Analysis of potassium dynamics in mammalian brain tissue. J Physiol. 1983;335(1):393–426.

66. Chen KC, Nicholson C. Spatial buffering of potassium ions in brain extracellular space. Biophys J. 2000;78(6):2776–2797.

67. Odette LL, Newman EA. Model of potassium dynamics in the central nervous system. Glia. 1988;1(3):198–210.

68. Newman EA. Inward-rectifying potassium channels in retinal glial (Muller) cells. J Neurosci. 1993;13(8):3333–3345.

69. Qian N, Sejnowski T. An electro-diffusion model for computing membrane potentials and ionic concentrations in branching dendrites, spines and axons. Biol Cybern. 1989;62(1):1–15.

70. Gleiser C, Wagner A, Fallier-Becker P, Wolburg H, Hirt B, Mack AF. Aquaporin-4 in astroglial cells in the CNS and supporting cells of sensory organs – a comparative perspective. Int J Mol Sci. 2016;17(9):1411.

71. Nielsen S, Nagelhus EA, Amiry-Moghaddam M, Bourque C, Agre P, Ottersen OP. Specialized membrane domains for water transport in glial cells: high-resolution immunogold cytochemistry of aquaporin-4 in rat brain. J Neurosci. 1997;17(1):171–180.

72. Chen KC, Nicholson C. Spatial buffering of potassium ions in brain extracellular space. Biophys J. 2000;78(6):2776–2797.

73. Lu YB, Franze K, Seifert G, Steinhäuser C, Kirchhoff F, Wolburg H, et al. Viscoelastic properties of individual glial cells and neurons in the CNS. Proc Natl Acad Sci. 2006;103(47):17759–17764.

74. Li Y, Konstantopoulos K, Zhao R, Mori Y, Sun SX. The importance of water and hydraulic pressure in cell dynamics. J Cell Sci. 2020;133(20):jcs240341.

75. Alnæs M, Blechta J, Hake J, Johansson A, Kehlet B, Logg A, et al. The FEniCS project version 1.5. Archive of Numerical Software. 2015;3(100).